Experimental and numerical investigation of the responses of scaled tanker side double-hull structures laterally punched by conical and knife edge indenters

Min Zhang [a,b], Jingxi Liu [a,b,*], Zhiqiang Hu [c], Yao Zhao [a,b]

[a] School of Naval Architecture and Ocean Engineering,

Huazhong University of Science and Technology, Wuhan 460074, China

[b]Collaborative Innovation Center for Advanced Ship and Deep-Sea Exploration(CISSE), Shanghai 200240, China

[c]School of Engineering, Newcastle University, Newcastle upon Tyne, NE1 7RU, UK

*Corresponding Author

e-mail: liu_jing_xi@hust.edu.cn

Tel.: +86 13638654101

ABSTRACT

This paper addresses experimental and finite-element simulation studies on scaled double-hull side structures quasi-statically punched at the mid-span by conical and knife edge indenters to examine their fracture behaviors and energy dissipation mechanisms. The specimen, scaled from a tanker double side, accounts for one span of the stringers in length and two spans of the web frames in width. The experimental results show that a double hull punched by a conical indenter shows much stronger resistance than that of a double hull punched by a knife edge indenter in severe collisions due to a difference in the fracture mode, while the double hull performs better in minor collisions punched by the knife edge indenter due to the deformation mode. In addition, numerical simulations are also carried out for the corresponding scenarios by the explicit LS-DYNA finite element solver. A relatively fine mesh in the contact area is used to capture the fracture initiation and propagation of the two specimens. The resistance-penetration curves and the deformations are compared with those observed in experiments, and these results match well. The numerical analysis discusses some aspects of particular relevance to the response of ship structures suffering accidental loads, including the importance of specifying the joining details, the influences of failure criteria, material relations on simulating complex structures, and application of scaling laws in assessing the impact response of full-scale structure.

Keywords: Collision; Double hull; Experiment; Numerical simulation; Deformation and fracture mode; Resistance-penetration response.

1. Introduction

Although ship collision avoidance systems and navigation tools have improved considerably in recent years, ship collisions still inevitably occur with increasing tonnage and busier traffic lanes. Once a tanker suffers a serious accident, the penetration of the inner hull involves cargo spillage, and disastrous long-term consequences, particularly environmental pollution that threatens the lives of marine organisms and human beings. Consequently, MARPOL and IMO have successively made it mandatory for tankers to be fitted with double hulls at a certain age [1]. Before rupture of the inner hull, the double hull structure can undergo complex dynamic responses that include crack propagation on the outer hull and a coupling effect between the structural members. Therefore, investigations of the response of double hull structures subjected to collisions are significant for reliable crashworthiness assessment in the pre-design state.

In general, the commonly used approaches to assess the internal mechanics of ship collisions can be categorized as experimental methods, numerical simulation methods and simplified analytical methods [2]. Among these approaches, experiments can provide reliable data to verify the other two methods. Previous trials have focused on full-scale collision and grounding experiments with the expectation of simulating real conditions (Netherlands) [3, 4]. However, those experiments are extremely expensive. Hence, model tests are usually applied to evaluate the crashworthiness of ship structures. Quasi-static indentation tests are usually applied to investigate the indentation response and damage mode of ship structures. Compared with the low-velocity impact model test, quasi-static indentation testing is relatively easier to conduct and is considered to provide a good reference for low-velocity impact loading situations [5]. Therefore, a host of quasi-static indentation tests were performed to evaluate the deformation and fracture mode of ship structures. For double hull structure punching experiments, a spherical or a conical indenter is usually selected to represent the bulbous bow in a side collision or the seabed obstacle in a stranding

scenario [6]. For example, Wang et al. [7] conducted series tests to shed light on the different behaviors of double hulls in a broad spectrum of collision and stranding scenarios. The results revealed that both the indenter size and the penetration location had a significant influence on the reaction force. Paik and Seo [8] utilized double hull punching experiments to validate an efficient method for progressive structural crashworthiness analysis. Karlsson et al. [9] developed four types of experiments, including bulb impact on double hull structures, to establish a reliable and robust FE modeling procedure for ship-ship collision simulations.

In fact, the accidental scenarios a ship may encounter during its sailing life are very uncertain, introducing substantial difficulties for crashworthiness assessments in the pre-design stage. Hence, the establishment of a performance-oriented standard is proposed for assessing the crashworthiness of ships' side structures compared with the majority of rules and regulations [10]. In the cases of ship bow-side collisions, the striking bow profiles that a ship may encounter are diverse. Moreover, the deformation modes and fracture mechanisms of structures impacted by differently shaped indenters can vary greatly. For instance, Jones et al. [11-13] proposed a theoretical method to predict the dimensionless perforation energy for plates struck by various indenter shapes, which illustrates that the indenter shape has a direct bearing on the energy absorption of a plate. Liu et al. [14] reported that the initial fracture of a plate impacted by a spherical indenter or a cylindrical indenter is caused by combined tension and compression or combined tension and shear, respectively. Nevertheless, previous studies have mainly concentrated on the impact responses of single plates. Furthermore, experiments on double hulls punched by various indenter shapes are insufficient. Moreover, as in the approval procedure suggested by Zhang et al. [15], at least two types of striking bow shape should be used to estimate the critical deformation energy during a ship collision. Therefore, the objective of the experiments in this study is to investigate the deformation modes and fracture behaviors of double hull structures punched by different indenters.

The non-linear finite-element method has the ability to predict the large deformation, collapse mode and reaction force of structures subjected to collisions when rationally provided with proper modeling parameters. Therefore, it is widely used to simulate marine structures in many fields of industrial engineering, such as safety calculations, security studies, hazard assessments and structural optimization. Moreover, numerical simulations can be treated as virtual experiments and are currently used extensively to validate simplified analytical methods in many collision and grounding scenarios [16-20]. Compared to model tests, numerical simulations are low cost and repeatable with the help of powerful computers. Furthermore, they can provide detailed information on each structural component, which gives insight into crashworthiness analysis. However, simulation results are sensitive to several factors, including mesh size, failure criteria and the definition of material relationships, as examined in previous benchmark studies [21-23]. Failure prediction using numerical simulation has proven to be a very difficult topic because the effective plastic strain to predict element failure is highly dependent on the element size, and discrepancies can be found in the prediction of ductile fractures in sheet metal when different failure criteria are applied [23]. Therefore, material failure should be validated against experimental tests before performing structural analyses. Moreover, the material relations that can simulate the strain hardening of ductile metal beyond local necking are numerous, and those commonly applied to simulate marine structures subjected to impact load are modified power law formulations [24], combined material relations [25], weighted material relations [26] and Voce material models [27]. Their influence on the simulation results should be discussed extensively. In addition, the boundary conditions simulated in a specific model test should adequately represent the experimental support condition whether in a quasi-static indentation test [5, 28, 29] or in a low velocity impact test [25, 30-32]. Therefore, the focus of the numerical simulation study is defining these influence factors properly, with the aim of developing a robust numerical simulation.

The motivation of this paper is to reveal the damage mode of a scaled double hull punched by conical and knife edge indenters through quasi-static penetration experiments and nonlinear numerical simulations. Another purpose of the model tests is to develop experimental data to validate the numerical method in simulating complex structures. This approach could enable the validated model to be used with confidence to predict the response of full-scale structures under various collision scenarios. The structure of the paper as follows:

(1) In Section 2, the experimental details are presented, including the design and manufacturing process of the double hull specimen, the material properties of the specimen, the experimental method to obtain the indentation responses and the experimental results.

(2) The numerical simulation is presented in Section 3. The description of the FE models and the material model utilized are presented. Special attention is paid to the boundary condition, the treatment of the modeled welds and the determination of the critical failure strain. Moreover, numerical results are analyzed with the experimental results in terms of the resistance-penetration response, the deformation process and the energy absorbed by each member in each test.

(3) In section 4, several factors that are related with the numerical simulations are discussed, including the modeled welds, mesh resolution, failure criterion, selection of material and scaling effects.

(4) Some conclusions are drawn, and suggestions for establishing a robust finite element model are presented in section 5.

2. Experiments

2.1. Specimen

The ship bow side collision scenario depends on the ship speed, collision angle, loading condition, draft, trim and striking bow geometry, as reviewed by Wang et al. [10]. Among these factors, the current study attempts to investigate the influence of

the striking bow geometry on the impact response of a double hull structure. Fig. 1 represents the collision scenario, in which a 16500 DWT oil tanker suffers a head-on collision on its side by two typical striking bows. According to Wang et al. [10], the striking bow geometry can be generally idealized as a wedge (raked bow) or a conical striker (bulbous bow) in model tests. It is recognized that ship bows are deformable to a large extent. But this paper aims to investigate the collapse behavior of the double hull, then ignoring the deformation of the bulbous bow can bring clear and conservative results. Therefore, two rigid indenters are designed to assess the different collapse modes and energy absorption mechanisms of the double hull structure over a wide range. As depicted in Fig. 2, the indenters consist of a conical indenter and a wedge indenter with a sharp tip, representing the blunt and non-blunt indenters, respectively.

The studied double hull includes one span of the stringers in width and two spans of the web frames in length; the span lengths are 3.6 m and 2.4 m, respectively. In addition, the distance between the double sides is 1.08 m. Thus, a one-sixth scaled specimen is designed, where the impact location is between the two stringers. The scaled geometry is also sketched in Fig. 1. To better clarify the five stiffeners on each side plate, the stiffeners located from the middle to the boundary are denoted the ‘central stiffener’, ‘lateral stiffener’ and ‘marginal stiffener’. The thickness of all the plates is 2 mm, and the stiffeners are 36×2 mm with a flat bar. It should be noted that the stiffeners on the web frames are smeared out by increasing the thickness of the attached plates in the small-scale specimens. With these scaled dimensions, the section modulus of the small-scale specimen is 10% smaller than the full-scale one. For reference, the main dimensions of the full prototype are provided in Table 1, and the scantlings of the structures are indicated in Table 2.

The material used for the plates and stiffeners is normal structural hot-rolled steel from a single batch supplied by the WISCO company (Wuhan Iron and steel (Group) Company, China). To obtain the mechanical properties of the steel, quasi-static tensile

tests are conducted using standard tensile specimens and procedures. The tension tests are conducted on materials cut from the plate that would be used to fabricate the double hull. The dimensions of the machined tension test pieces are shown in Fig. 3. Three tensile tests are performed for each parent plate at a rate of 2 mm/min until fracture occurs. Based on the displacement-controlled tensile tests carried out on the machine Zwick/Roll Z010, the engineering stress-strain behavior of the material can be obtained. The equivalent stress-strain relationship is represented by a modified power-law relation.

$$\sigma_{eq}=\begin{cases}\sigma_Y & \text{if } \varepsilon_{eq}\le\varepsilon_{plat}\\ K\left(\varepsilon_{eq}+\varepsilon_0\right)^n & \text{otherwise}\end{cases} \tag{1}$$

where σ_{eq} and ε_{eq} are the equivalent stress and the equivalent strain, respectively. σ_Y is the initial yield stress, and ε_{plat} denotes the equivalent plastic strain at the plateau exit. The strain ε_0 allows the plateau and power law expressions to intersect at (ε_{plat}, σ_Y). K and n are the strengthening coefficient and strain-hardening index of the material, respectively. The latter three material parameters, ε_0, K and n, are obtained through curve fitting of the true stress-strain relation prior to local necking derived by the formulae proposed in Ref. [33]. Moreover, the mechanical properties of the plate material are summarized in Table 3, and the tensile stress-strain curves are presented in Fig. 4.

To fix the scaled double hull, a ring frame that is welded together by 18b channel steel [34] is applied, and its material properties are summarized in Table 4. The section profile of the channel steel is transformed into a flat plate, which shares a similar moment of inertia and sectional area so that it can be modeled in numerical simulation in future work, as plotted in Fig. 5. The top and bottom surfaces of the frame are polished to guarantee uniform flatness. A number of holes with a diameter of 22 mm are drilled on them for further assembly and fastening. Specific locations on the frame are welded with stiffeners 10 mm in thickness designed by numerical simulation to ensure adequate strength. Moreover, there is a 40-mm-diameter circular

hole on each side of the frame to capture the deformation details of the inner components in the experimental process. Fig. 6 illustrates the dimensions of the specimen, as well as the relative positions of the stiffeners and observation holes. Furthermore, the manufacturing process of the specimens is depicted in Fig. 7. In Fig. 7(a), electrode arc welding is applied to connect the ring frame with the inner components of the double hull. A GB: E-4303 electrode with a 1.2 mm diameter is selected [35], and the corresponding filled weld leg is between 2 mm and 3 mm in width. Fig. 7(b) depicts the slight computer-numerical-control (CNC) laser marking on the side plates to determine the future laser welding path as drawn by the red dashed lines. Moreover, slots are CNC-cut on the plates to mate with the teeth on the stiffeners shown in Fig. 7(a). In Fig. 7(c), the upper and lower face panels are successively connected with the inner members and the ring frame by laser welding, as marked by the red and green lines. In addition, the green lines indicate that electrode arc welding is used to strengthen the connection between the upper panel and the attached middle three stiffeners, as well as the web frame, with the aim of avoiding unsoldering when this region experiences excessive folding and tearing [36].

2.2. Set-up

The experiments are conducted at Huazhong University of Science and Technology. The test rig is presented in Fig. 8. The specimens are clamped between a bottom flange and an upper flange, which are made of No. 45 steel with a thickness of 20 mm. They are fixed together by M20 bolts. The deformation of the double hull structure is enforced at a rate of ~10 mm/min on the middle span by two hydraulic cylinders, which are series connected to obtain enough loading distance. The two indenters described above are used to represent two impact scenarios, in which the specimens punched by a conical indenter and a wedge indenter are denoted S-C and S-W, respectively. A 100-ton load cell fixed between the hydraulic cylinder and the indenter and two displacement sensors jointed on the indenter are utilized to obtain the force-time and displacement-time curves, respectively. The experimental process is

recorded by a standard video camera. Additionally, a digital microscope is adopted to monitor local deformation of the inner components from the observation holes. To visualize the deformations, 50×50 mm grids are drawn on the front and rear sides. The entire indentation process includes the punching of both the outer and inner stiffened panels. After the resistance force of the inner hull declines rapidly, the test stops after the specimen is punched for another ~30 mm.

2.3. Experimental results

The permanent deformations of the specimens are shown in Fig. 9. The openings in the specimens assume the shape of the indenters, and the components beneath the indenters experience large deformation and tearing. Moreover, the plastic behavior of the specimens throughout the whole indentation process can be well described by the resistance-penetration response, see in Fig. 10, where two peak values are captured in each model test when the side plates take effect. Beyond these values, the stiffened plate will completely collapse. The recorded values of the penetrations and the deformation energies corresponding to the peak forces, as well as the forces corresponding to each tearing process are summarized in Table 5 for the two specimens, where deformation energy is obtained by the integration of the area beneath the curve of resistance vs. penetration, i.e., Fig. 10. Specimen S-W exhibits less energy dissipation ability, especially at the first peak, where the values of the penetration and absorbed energy are nearly one third those of specimen S-C. At the second peak, the ratio reaches approximately half for the energy dissipation due to the similar tearing force, which consumes a fixed amount of energy.

Moreover, the collapse processes are divided into four stages according to the main contributing components and deformation mechanisms. Fig. 10 only depicts the stage division of specimen S-W, in which stage 1 and stage 3 indicate the performance of the outer and inner stiffened plates from contact to collapse, respectively, and stage 2 and stage 4 are the two tearing processes. The tearing processes in specimen S-C are not evident. Moreover, the observations of the penetration process are summarized in

Table 6 in the order that they are described in the text.

In stage 1, the outer stiffened panel plays the main role. At the initial time, the indenters contact the specimens, and the stiffened panels mainly suffer elastic bending, while the elastic limit of specimen S-C is approximately one third that of specimen S-W. This result is observed because bending dominates the resistance and the numbers of stiffeners directly beneath the wedge and conical indenters are three and one, respectively. With the indentation, the plate behavior transforms from bending deformation to membrane stretching, and the resistance forces grow continuously. During this process, it can be found that the slope of the resistance-penetration curve in specimen S-C is smaller than that of specimen S-W, which indicates that the side plate of a ship could provide stronger resistance when impacted by a wedge-like object than when impacted by a conical one in a minor collision. Nevertheless, in the case of a severe collision, the energy dissipation ability of specimen S-C is much better for a larger critical indentation depth due to the difference in the fracture mechanism. In addition, the large in-plane compressive load from the side plate can trigger the buckling of the web frame. Thus, the collapse of the outer stiffened plate is delayed, as shown in Fig. 11(a). This phenomenon is different from that of previous experiment in which the surrounding girder webs are assumed to be stiff enough to restrict the membrane force without deforming [37].

The crack initiation and propagation of outer stiffened panels laterally punched by conical or wedge indenters have been extensively investigated in previous studies [28, 37-39]. Similar observations can be discovered where the cracks are initiated at the end corners of the wedge in specimen S-W, while plate thinning results in fracture in specimen S-C. Moreover, in specimen S-C, the rupture of the side plate leads to a decrease of the resistance force, but it will not decrease until the stiffened plate is torn open in specimen S-W. During this stage, the performances of the central stiffeners in the two specimens can also vary greatly, as shown in Fig. 12. The central stiffener in specimen S-C mainly suffers global bending and tension, and a crack is formed due to

crack transmission from the side plate. In contrast, fracture is triggered by excessive local bending and tension in specimen S-W. Moreover, the failed stiffeners do not trip before undergoing fracture, which is different from some other experimental observations [28, 37]. This phenomenon may arise from the electrode arc welding providing additional material, resulting in an increase in tripping resistance. Another factor is that the ends of the stiffeners are constrained by the web frames, which can release some in-plane load from the stiffeners. When the stiffeners are loaded symmetrically, they do not trip to either side.

Compared with the outer stiffened panels, there are many differences in the responses of the inner stiffened panels, which are attributed to the fact that the indenters contact the stiffeners prior to the plates. An abrupt increase in the resistance force occurs at a displacement of ~144 mm, as illustrated in Fig. 10, indicating that the inner stiffened panels dominate the resistance in stage 3. The corresponding performances of the stiffeners in the two specimens are distinct. According to Fig. 10, the resistance-penetration curve of specimen S-W fluctuates twice when the stiffeners suffer denting. From the final deformation (Fig. 9 (b)), there is slight folding at the edges of the stiffeners, which reveals that the stiffeners could experience local folding and subsequent cutting. The two peak values of the curve are the buckling and initial tearing limits of the stiffeners. Stiffener folding can also be found in specimen S-C (Fig. 9(a)), and the crack observed can initiate from the folded stiffener. This process differs from the phenomenon observed on the outer plate, where a circular plate is punched off from the side plate coincident with the path of the necking circle. Moreover, it should be noted that the maximum reaction force of the inner plate is higher than the outer plate in specimen S-C, while the case is opposite in specimen S-W. This difference reveals that the failure of the inner plate in specimen S-C could also mainly be attributed to tension failure despite the influence of the collapsed stiffener, while the failed stiffeners could cause premature fracture in specimen S-W. At the moment when the wedge contacts the inner plate, there is gap between the

wedge and plate that is mostly filled with the collapsed stiffeners, which act as obstructions. Thus, the contact surface no longer has the form of a line. Therefore, the stress concentration at the two end corners of the wedge is increased. Then, the fracture is initiated, and the plate is further directly torn open. Another detail that is observed in specimen S-C is that the end of the central stiffener in specimen S-C is fractured due to excessive tension and torsion, as depicted in Fig. 11(b).

Stage 2 and stage 4 encompass the tearing processes in which the contributed energy dissipation is relatively small compared with the membrane tension effect of the stiffened panels. The tearing in specimen S-W originates from the cutting of the four oblique edges of the wedge indenter, as well as the rolling of the stiffened plates under the two inclined planes. While the situation in specimen S-C is different, the cracks on the plate will propagate along the adjacent stiffeners or drive them to fracture with the punching of the indenter (Fig. 9(a)). The resistance is generated from the vertical pressure and tangential friction between the contact surfaces.

3. Numerical simulations

3.1. Numerical models

The computations are implemented in the LS-DYNA R7.0 explicit finite element package [40]. Fig. 13(a) shows the schematic diagram of the finite element model, which consists of the specimen, bottom flange, upper flange and indenter. The indenters are -2 mm offset in the y-axis direction from the central position, considering that the structural strength on each side of the indenter cannot be perfectly equal in the model test. All the components are discretized into reduced integration shell elements with five integration points through the thickness, defining the Belytschko-Lin-Tsay shell element formulation. Special attention is paid to the spatial discretization of the double-hull structures in the specimen. The area limited by the two marginal stiffeners and the two web frames is meshed with an element size of 2 mm (le/t=1) to predict the plate fracture and crack propagation correctly. Here, le is the element length, and t is the thickness of the element. The mesh size is 4 mm for

the web frames, and the remaining elements are modeled with a coarse mesh of 6 mm. A more coarser mesh with a 10-mm element size is used to model the channel steel frame, the lower flange and the upper flange, with the aim of decreasing computation time. Furthermore, the indenters are mapping meshed, and their tops are meshed with an approximately 3 mm element size to avoid mesh penetration. Hourglass stiffness is added to the reduced integration elements using the stiffness-based form [41].

The weld joints are accounted for in the simulations by increasing the plate and stiffener thicknesses at their intersections. This measure is necessary because the weld increases the tripping resistance of the stiffener in the model test (Fig. 12). The height and width of the electrode welding beam are between 2 mm and 3 mm. Moreover, the effect of laser welding is considered by adding 1 mm thickness to the plate. Laser welding is only considered for the central three stiffeners between the web frames. Therefore, the welds are represented by a row of 3 mm wide elements with increased thickness. Their final thicknesses are illustrated in Fig. 13(b).

Fig. 13(c) depicts the boundary conditions in the numerical model that aim to replicate the real circumstances of the experiments. The contact between the indenter and the specimen and the contact that occurs between structural components during the indentation process are defined as a single-surface contact algorithm. The double hull and the channel steel are merged to a single entity because they are welded together in most locations (Fig. 7). The contact between the specimen and the upper or lower flange is defined as the surface-to-surface contact algorithm. The static coefficient of friction is set as 0.3, and the dynamic coefficient of friction is omitted for all the defined contacts [24]. In particular, special gaps are defined between the slave and contact surfaces to avoid contact penetration [41]. The specific values are also illustrated in Fig. 13(c). Moreover, at the positions clamped by the upper bolts, nodes on the upper flange and the specimen are coupled in *Tx*, *Ty* and *Tz* degrees of freedom. At the locations fastened by the lower bolts, the nodes on the specimen are constrained in *Tx* and *Ty* degrees of freedom.

Fracture prediction is of utmost importance for the numerical simulation of ship collision events. Based on the study by Calle et al. [23], good performances to model failure in tension coupons designed with a wide range of triaxialities can be reproduced if the element length thickness ratio is less than or equal to 2 by applying four commonly used failure criteria, including the Equivalent Plastic Strain criterion (EPS), the Germanischer Lloyd criterion (GL), the Rice-Tracey-Crockroft-Latham criterion (RTCL) and the Bressan-Williams-Hill criterion (BWH). Moreover, the EPS criterion is used for its convenience compared to move advanced criteria [28, 29, 42, 43]. To obtain the 'critical failure strain' of the material, which is intended to predict the fracture of the double hull, numerical simulations of the uniaxial tensile test were conducted. The simulated engineering stress-strain curve is plotted in Fig. 14. Thus, the critical failure strain for the double hull (side plate and stiffeners) is estimated to be 0.57. The corresponding material selected from the library of LS-DYNA is 'Mat_123_Modified piecewise linear plasticity', which is available for enhanced failure criteria. In particular, a rectangular plate and an attached stiffener measuring 80 mm in the y-axis direction and 50 mm in the x-direction is defined as having failed when the lateral indentation of the conical indenter reaches 135 mm, with the aim of removing the interference of the structure failed from outer stiffened plate along the necking circle. The material used for the channel steel frame is 'Mat_003_Plastic kinematic', based on its potential deformation. An elastic material ('Mat_002_Elastic') is applied to model the upper flange, and a rigid material ('Mat_020_Rigid') constraining all degrees of freedom is defined to simulate the bottom flange. Furthermore, the rigid material used for the indenter is different to release constraints in the 'z-axis' direction. All rigid materials are assigned mild steel mechanical properties.

Moreover, in order to evaluate the factors that could influence the simulation results of scaled specimens and the collapse behaviors of ship structure in a full-scale prototype, a number of additional numerical simulations are performed. These

additional simulations include: a FE model where the added thickness at the weld seams are not considered to assess the influence of the modeled welds; simulations for different element sizes (le/t=1, 2, 4, 8) and various failure criteria (EPS, GL and RTCL); simulations for material relations with different strengthening effect; and full-scale FE models with and without modeled welds to investigate the features provided by the model tests and numerical simulations of scaled specimens can be observed. The full-scale models are geometrically similar scaled from the small-scale ones with scale factor β=1/6, involving indenter sizes, plate scantlings and thicknesses [52]. Moreover, in the FE model, the material relation is the same as that in the small-scale model. The element size and element thickness are all 12 mm. Thus, le/t remains to be 1 and the corresponding fracture strain is unchanged.

3.2. Numerical results

The numerical resistance-penetration responses are compared with the experimental results in Fig. 15. The plastic behavior and tendency of the impact responses are well forecasted by the numerical simulations. Slight discrepancies can be found in the regions close to the peak values. Moreover, disparities can also be discovered in the tearing stages, in which the numerical results are relatively higher than the experimental ones. Generally, failure prediction in numerical simulation is challenging. The fracture modes in these two experiments are complicated, including plate tension failure, plate shear failure, plate tearing failure and in-plane denting failure. However, only one failure strain fails to predict all the effects precisely. In addition, the deviation of predicted resistance from the experimental one in the tearing process is difficult to explain and will be put in our future work. Nevertheless, the numerical results could provide an adequate reference for the deformation processes of the specimens, which are difficult to capture in model tests because they are surrounded by stiffened channel steel. To describe the process, several moments of the resistance-penetration curves are taken into account. At the same time, the deformation modes found in the experiments are thoroughly compared with those in

the numerical simulation. Moreover, the deformation processes and comparison results of specimens S-C and S-W are summarized in Table 7 and Table 8.

For specimen S-C (Fig. 16), at the elastic limit, the upper stiffened plate experiences a displacement of approximately 1.5 mm as a consequence of a very local indentation where the resistance mainly originates from the bending of the central stiffener (step a). Beyond this point, the side plate suffers membrane tension, and the central stiffener sustains combined tension and bending (step b). With the indentation, the web frames can provide two opposite supports to the stiffened plate, and their in-plane force increases gradually. Fig. 15(a) illustrates that the resistance-penetration curves bifurcate slightly in this process, which demonstrates that the effect of the web frame in numerical simulation is slightly stronger. When the in-plane force exceeds the ultimate buckling load of the web frame, a bulge forms outward with the vertical push from the stiffeners at a lateral indentation of approximately 90.5 mm (step c), see in Fig. 16(c).

With the indentation, fracture emerges on the plate, immediately contributing to a rapid load decrease (step d). Tripping never occurs on the central stiffener in previous steps. Thus, stress concentrates on the reverse-curvature of the stiffener edge, and failure occurs at this point. This result corresponds to the experimental observation in Fig. 12(a). At a displacement of approximately 99 mm (step e), a breach on the stiffener is triggered by the fractured plate, resulting in a large hole on the side plate. Subsequently, the cracks expand along the necking circle, and the top of the plate is pushed aside.

At a displacement of approximately 144 mm, the indenter contacts the inner central stiffener. The central stiffener initially experiences local folding, which can induce global tension on the attached plate at the same time (step f). The numerically predicted resistance is below the experimental resistance because the edge of the stiffener can supply a greater contact area when the conical indenter contacts the stiffener in the experiment than in the numerical simulation. Meanwhile, in this step,

two cracks initiate on the outer plate near each stiffener and propagate along them. As the indenter displacement increases, a plastic hinge forms at the root of the central stiffener, and the stiffener is pushed down gradually. Moreover, two cracks initiate on the stiffener due to excessive folding.

At a displacement of 223 mm, the central stiffener trips down and finally contacts the inner plate (step g). However, bifurcation of the resistance-penetration curves is observed again after this point because the central stiffener is fractured; thus, its tension effect is weakened. Moreover, the initiation of a defect on the stiffener can give rise to earlier fracture of the side plate. As shown in step h, the failure of the side plate is mainly attributed to the cracked stiffener permitting a lower peak force than that observed in the first peak. Finally, the inner stiffener plate is torn open. Unlike the model test (Fig. 9(a)), no crack is found along the stiffener. Attention should be paid to the process in which cracks propagate fully along the adjacent stiffeners from step f to step h, and the stiffener crack does not develop. This result differs from the phenomenon shown in Fig. 9(a), which indicates that the intersections of the plate and stiffener connected with both laser welding and electrode arc welding are relatively brittle. One detail that should be mentioned is that the two ends of the central inner stiffener fail due to exaggerated tension (Fig. 17), which is similar to the experimental observation in Fig. 11(b).

For specimen S-W (Fig. 18), there are many differences from the deformation of specimen S-C. Elastic bending can be observed in the initial stage (step a), where the contributing members are the middle three stiffeners. Strain concentrates on the two end corners of the wedge indenter, and fracture appears here with gradual loading (step b). At the same time, decreasing resistance is observed in the resistance-penetration curve (Fig. 15(b)), while no disturbance is found in the experimental response. This phenomenon is similar to observations reported in Ref. [28] and can be attributed to the sudden disappearance of elements. After that, the indenter cuts open the outer plate along its top line (step c). Meanwhile, the resistance

force drops abruptly. In step d, Fig. 18(d) gives the strain distribution of the stiffeners, where the concentration runs diagonally from the top of the indenter to the edge of the stiffener. This observation resembles the fracture mode shown in Fig. 12(b).

Step e shows the typical tearing state of the outer stiffened plate. Each part of the plate underneath the two inclined planes of the wedge rolls with indentation, and the two sides of each plate are gradually torn off. Fig. 15(b) reveals that the tearing force declines at some points according to both the experiment and simulation results. In fact, a constant force is usually applied to assess the tearing resistance of a plate when assuming a constant value of the tearing length [44]. In the present analysis, the effect of the stiffeners should not be neglected. When the outer stiffened plate is torn open, initial folding deflection emerges on the attached stiffeners due to the bending effect. With the rolling of the plate, the folding resistance may diminish gradually, decreasing the total tearing resistance. Note that no buckling is found on the web frames in previous steps, which differs from the situation in specimen S-C.

Moreover, at step e, an abrupt increase in the resistance force emerges, illustrating that the inner stiffener plate suffers lateral indentation. The three stiffeners are directly cut off by the sharp edge of the indenter, and the resistance force increases progressively. This phenomenon does not conform to the deformation mode in the model test described previously (Fig. 9(b)). This difference can also be explained, as in the case of specimen S-C, by noting that the thickness of the stiffener in the numerical simulation cannot be considered; thus, the contact between the wedge indenter and the stiffener is ‘point contact’, while it is ‘line contact’ in the experiment. The latter case would be expected to provide more resistance, and the former scenario leads to immediate shearing failure when the element exceeds its limit. When clear inner plate fractures occur at the two end corners of the indenter, the resistance force reaches its peak value (step f). After that, it decreases rapidly because the whole inner stiffened plate is torn open immediately (step g), which is distinct from the case of the outer stiffened plate (step b).

The deformation and fracture characteristics of the two double hull specimens can be described according to the structural deformation process. Their deformation and failure modes are quite different, clearly distinguishing their energy absorption ability. Specimen S-W suffers severe local shearing that causes earlier plate failure compared with specimen S-C, which mainly experiences uniform tension failure. Moreover, the resistance of the inner stiffened plate is different from that of the outer plate because the damaged stiffeners attached to the inner plate influence the fracture initiation of the side plate. In general, the distinctness of the failure mode and interference of the members introduce many challenges in numerical simulations.

Another advantage of numerical simulation is that it can conveniently obtain energy dissipation by all individual members. Fig. 19 shows the accumulated internal energy in the outer stiffened plate, the inner stiffened plate and the web frame during the indentation. It is evident that some energy can be absorbed by the web frame in specimen S-C due to its large plastic bending. Thus, the in-plane displacement of the web frame indicates that a larger deformation area develops on the outer stiffened plate than the inner one, resulting in much more critical deformation energy, as shown in Fig. 19(a). The distinction is comparatively smaller in specimen S-W because little deformation occurs on the web frame.

The critical indentation depth of the outer and inner stiffened plates can also differ in each case. Therefore, it is difficult to predict the failure of the double hull structure analytically because only a simple formula has been utilized to predict plate fracture [17, 45-47]. Moreover, the energy absorbed by the outer stiffened plate increases steadily after plate fracture arises in both specimens. In this process, the outer stiffened plate suffers tearing, and the corresponding absorbed energy is remarkable, especially in the case of specimen S-W. Although the tearing process is not simulated well by the finite element method, as shown in the experimental and numerical comparisons in Fig. 15, i.e., the data produced may have deviations, demonstrating that the resistance in the plate tearing process could contribute a significant portion of

energy and should be further studied.

4. Discussion

4.1. Influence of modeled welds

In the present numerical model, the weld seams are accounted for by adding plate thickness to the plate-stiffener intersections. How the added thickness influences the simulation results is evaluated in this section.

In the simulation of specimen S-C (Fig. 20(a)), the lack of definition for the weld elements results in many disparities in the resistance force during the indentation process. These disparities mainly occur because the modeling of the weld seam can provide a rotational constraint in the deformation process. At moment *t1*, the central stiffener attached to the outer plate trips down, and no fracture generates at that point. Thus, the stiffener and the connected plate can supply some tension resistance. At moment *t2*, the folding resistance of the central stiffener attached to the inner plate is underestimated. At moment *t3*, the excessive rotation at the intersection of the stiffener and the plate can lead to their separation. Thus, the resistance force drops earlier when the welded element is not considered. In contrast, the influence of welding is relatively small in specimen S-W (Fig. 20(b)) since the added thickness on the plate and stiffeners can increase an extent of resistance.

The method used to consider the effect of welding in the present analysis has been generally applied. For the stiffened plate, the addition of welds confers increased in tripping resistance and a smoother cross-section transition between the stiffener and plate [24]. Moreover, for the stiffened web girders, welding can provide axial restraint when the girders are loaded vertically. The deformation shape and buckling resistance are closely related to the structural joining details [29]. In the present numerical simulation of scaled double hull punched by a conical indenter, the addition of a weld greatly influences the deformation pattern and fracture mode of the structure.

4.2. Mesh resolution and the failure criterion

It is crucial to define the failure criteria to predict the rupture of ship structures in numerical simulations of collision and grounding. The commonly used failure criteria to predict rupture of marine structures in collision accidents are the EPS criterion, the GL criterion, the RTCL criterion and the BWH criterion, as reviewed in the 'latest' benchmark study [23]. The former three criteria are selected to evaluate the impact response of the double hull as they have been implemented in "Mat_123" in Ls-dyna R7.0. Moreover, in accordance with the conclusion of another benchmark study, the element length is more important than the failure criteria themselves [21]. Therefore, numerical models with different element length-thickness ratios and failure criteria are used to simulate experiments.

The failure criteria are first calibrated by static tension testing. Fig. 21(a) shows the simulated engineering stress-strain curves of four typical element sizes. This result demonstrates that larger element size corresponds to increased element stiffness. Thus, necking is not obvious, and the failure strain gradually decreases with larger elements, as shown in Fig. 21(b). The obtained failure strains corresponding to a series of element length thickness ratios are curve fitted with a third-order polynomial [22]. It should be noted that the application of the RTCL criterion only requires the implementation of the failure strain in LS-DYNA; hence, the relevant parameter is not included in Barba's law. Subsequently, element sizes of 2 mm, 4 mm, 8 mm and 16 mm (le/t=1, 2, 4, 8) are chosen to simulate the two model tests.

Fig. 22 gives the simulation results. One similarity of the three failure criteria is that when predicting the fracture of the outer plate, the fracture moments in specimen S-C occur earlier with larger elements, while opposite predictions are found in specimen S-W. This phenomenon illustrates that it is difficult to use only one failure strain to forecast the two cases simultaneously with an uniform element size, and it is demonstrated that the best case for simulating the two scenarios is when the element length thickness ratio is equal to 1. The current Barba's law is calibrated based on

uniaxial tension test, not considering the effect of stress state, which can give rise to discrepancies in simulations with different mesh sizes [42, 48].

In regard to the inner plate, the rule considered above can be observed in specimen S-W, while the situation in specimen S-C is different. The resistance forces drop quite early in the results predicted by the GL and RTCL criteria. Their failure modes are shown in Fig. 23(a). The intersection of the plate and the central stiffener is prone to failure when the GL and RTCL criteria are used. However, it differs from the deformation shape predicted by the EPS criterion, as shown in Fig. 23(b), where the fracture is triggered by the folded stiffener and further indentation leads to the fracture of the plate along the stiffener. Therefore, the EPS criterion can better forecast the failure of the inner stiffened plate in the current scaled experiments.

4.3. Influence of material relation

The steel plate used in ship construction can experience local necking, which makes numerical simulations difficult. A number of plastic material relations can be applied in simulating the large deformation to fracture of structures in collision accidents, as discussed in the introduction. The disparities of stress-strain relations in large strain can lead an extent of difference to the calculation results. To evaluate the influence of the material relation on the simulation results, three different material curves are adopted to simulate the two model tests with the same mesh size (le=2 mm). The material curves are determined by the combined relation modified by Ling [26]:

$$\sigma_{eq} = w \cdot K\left(\varepsilon_{eq} + \varepsilon_0\right)^n + (1-w) \cdot \left[k\left(\varepsilon_{eq} - \varepsilon_u\right) + \sigma_u\right] \qquad \varepsilon_{eq} \geq \varepsilon_u \quad (2)$$

where σ_u and ε_u are the true values of the stress and plastic strain at the point where necking is initiated, k is the slope at this point, and w is the weighted value.

The combined material relation is the weighted average of the tangent-type and modified power-law relations. The selected three curves are w=0, 0.6 and 1, and the simulated uniaxial tension results are depicted in Fig. 24. The evolution rule resembles the case in which a type of material is simulated with various mesh sizes

(Fig. 21(a)).

The simulated resistance-penetration responses of the two experiments are plotted in Fig. 25. Only a slight distinction can be found in specimen S-W, which may be the reason that the stress concentration is severe in this case and the distribution of large strains on the plate beyond necking distributed is limited. Thus, the simulated curves are very close. In contrast, the strain gradient caused by the conical indenter in specimen S-C is moderate, resulting in a discrepancy in the resistance-penetration responses. If the weighted value w is lower, the hardening phase of the material is stronger. Thus, the reaction force is larger under conditions of large deformation, as shown in Fig. 25(a). Moreover, the moment of plate rupture is clearly delayed when w is equal to 0, while the other two are similar. This discrepancy can be attributed to the larger reaction force, which causes different deformation patterns where the central stiffener trips down and the web frame exhibits greater out-of-plane displacement (Fig. 25(c)). Thus the strain hardening of the material can influence the deformation mode of the double hull structure substantially when indented by a blunt indenter.

4.4. Scaling effects

The resistance-penetration responses for the full-scale prototypes are shown in Fig. 26, including the models with and without added welds, and simulation results scaled from the small-scale models according to the elementary scaling principles [52]. In the scaling laws, the geometric scale factor for a model is

$$\beta = \frac{l}{L} \tag{3}$$

where l and L are the lengths of small-scale model and full-scale prototype, respectively. And the force on the boundary of a model is related to

$$p = \beta^2 P \tag{4}$$

where p and P are the forces of small-scale model and full-scale prototype.

Therefore, the penetration depth (including the critical penetration depth) are scaled by $1/\beta$, and the resistances are scaled by $1/\beta^2$. This scaling law is applicable when

structural behavior involves little or no fracture and the strain sensitivity of the material is ignored [53]. Nevertheless, current numerical results contain significant portion of crack propagation behavior. Nevertheless, as stated by Liu et al. [39], there are no techniques available to extrapolate the fracture process of scaled model to full scale prototype so far. Therefore, the scaled resistance-penetration curves are taken as references as there should be deviations for the resistances in the tearing processes.

According to Fig. 26, it can be found that the main features simulated with and without modeled welds in full-scale structure are similar to that in scaled specimens, as the trends of the response curves match with that in the numerical results of testing specimens (Fig. 20). One distinction is at moment *t* in the structure punched by the conical indenter. The central stiffener attached to the inner plate is not fractured. Thus the tension effect can lead to the result of resistance increasing. In general, it demonstrates that the deformation and failure modes in full-scale structure can be forecasted by the small-scale model tests, and modeling of welds can also influence the impact response in full-scale model cases greatly.

Besides, the response curves scaled from small-scale model correspond well with that simulated with full-scale model. It illustrates that the results of small-scale model can be extrapolated to the full-scale prototype according to the elementary scaling laws. However, the well corresponded curves show that the numerical predicted crack propagation resistance also conforms to the scaling laws, which has been proved to be incorrect [54]. Moreover, it has been stated that the resistance in the tearing process is not predicted well in the current numerical simulation, see in Fig. 15. Therefore, the out-of-plane tearing behavior of ship side plate including the appropriate simulation techniques and scaling laws should be further studied.

5. Conclusions

The experiments and simulations of the double hull structures subjected to transverse indentation by conical and knife edge indenters serve to identify the large deformation and failure of complex ship structures. The finite element simulations,

considering the detailed boundary conditions and structural collecting details, predict the resistance-penetration responses and damage modes well.

The critical deformation energy absorbed by a double hull punched by a conical indenter is much higher than that of a double hull punched by a knife edge indenter, while the latter exhibits higher resistance in a minor collision. In addition to the differences in the deformation and fracture modes of side plates that lead to disparities, the buckling of the web frame can also dissipate collision energy.

The modeled welds play a very important role in terms of the resistance-penetration responses and fracture modes of the double hull structure punched by conical and knife edge indenters. For the outer stiffened plate, the rotational resistance between the plate and the stiffener provided by the modeled welds can avoid tripping of the stiffener, which further influences the fracture mode of the side plate. For the inner stiffened plate, the rotational resistance can improve the in-plate resistance of the stiffener, and the added weld can prevent failure at the intersection.

The experiments are simulated with three failure criteria (RTCL, GL, EPS) and various element sizes. For the outer stiffened plate, element failure appears earlier with larger element size when the double hull is punched by a conical indenter, and the opposite result is observed in the specimen indented by a knife edge indenter. For the inner stiffener, simulations with RTCL and GL criteria didn’t predict the failure well. Among them, EPS criterion with a small element size (le/t=1) can provide reasonable results for the current scaled model tests. Nonetheless, the tearing processes are not well forecasted. Further work should establish a criterion that can predict the initiation of plate fracture and the tearing resistance simultaneously.

In the numerical simulation of the indentation of a double hull structure, the resistance response is related to the strengthening of the material under large strain. A greater strengthening effect can result in a larger resistance force for the double hull structure and could further influence its deformation and damage mode due to the coupling effect of the structural members.

Based on the elementary scaling laws, numerical simulations of testing scaled specimens can give a good reference of collapse behaviors for the full-scale structures. And the results of small-scale model can be extrapolated to the full-scale prototype, except the resistance in the crack propagation process, which should be further researched on its scaling law.

Acknowledgements

The present work is supported by the National Natural Science Foundation of China (Grant Nos. 51579110 and 51609089) and the Fund project Independent Innovation Research Fund of Huazhong University of Science and Technology (Grant No. 2015TS004).

References

[1] International Maritime Organization. Construction requirements for oil tankers - double hulls. 2011.

[2] Hong L. Simplified analysis and design of ships subjected to collision and grounding PhD thesis. Norway: NTNU; 2008.

[3] Carlebur AFC. Full-scale collision tests. Saf Sci 1995;19:171–8.

[4] Wevers LJ, Vredeveldt AW. Full scale ship collision experiments. 1998. p. 260. TNO-report 98-CMC-R1725, Netherlands, Royal Schelde, The Netherlands: TNO; 1999.

[5] Gruben G, Sølvernes S, Berstad T, Morin D, Hopperstad OS, Langseth M. Low-velocity impact behaviour and failure of stiffened steel plates. Mar struct 2017;54:73–91.

[6] Amdahl J, Kavlie D, Johansen A. Tanker grounding resistance. In: Kim H, Lee JW, editors. Proc. 6th International symposium on practical design of ships and mobile Unit, vol. 2. Seoul, Korea: Society of Naval Architects of Korea; 1995. p. 1072–83.

[7] Wang G, Arita K, Liu D. Behavior of a double hull in a variety of stranding or collision scenarios. Mar Struct 2000;13(3):147–87.

[8] Paik JK, Seo JK. A method for progressive structural crashworthiness analysis under collisions and grounding. Thin-walled Struct 2007;45(1):15–23.

[9] Karlsson U, Ringberg JW, Johnson E, Hoseini M, Ulvfarsson A. Experimental and numerical investigation of bulb impact with a ship side-shell structure. Mar Technol 2009;46(1):16–26.

[10] Wang G, Spencer J, Chen Y. Assessment of a ship's performance in accidents. Mar struct 2002;15(4):313–33.

[11] Jones N, Birch RS. Low velocity perforation of mild steel circular plates with projectiles having different shaped impact faces. J Press Vess Technol 2008;130(3):031205.

[12] Jones N, Birch RS, Duan R. Low-velocity perforation of mild steel rectangular plates with projectiles having different shaped impact faces. J Press Vess Technol 2008;130(3):031206.

[13] Jones N, Paik JK. Impact perforation of aluminium alloy plates. Int J Impact Eng 2012;48:46–53.

[14] Liu B, Villavicencio R, Guedes Soares C. Shear and tensile failure of thin aluminium plates struck by cylindrical and spherical indenters. Ships and Offshore Structures 2015;10(1):45–58.

[15] Zhang L, Egge ED, Bruhns H. Approval procedure concept for alternative arrangements. In: Society of Naval Architects of Japan, editor. Proceedings of the 3rd international conference on collision and grounding of ships: Izu, Japan; 2004. p. 87-96.

[16] Gao Z, Hu Z, Wang G, Jiang Z. An analytical method of predicting the response of FPSO side structures to head-on collision. Ocean Eng 2014;87:121–35.

[17] Sun B, Hu Z, Wang G. An analytical method for predicting the ship side structure response in raked bow collisions. Mar struct 2015;41:288–311.

[18] Yu Z, Hu Z, Wang G. Plastic mechanism analysis of structural performances for stiffeners on bottom longitudinal web girders during a shoal grounding accident.

Mar struct 2015;40:134–58.

[19] Hu Z, Amdahl J, Hong L. Verification of a simplified analytical method for predictions of ship groundings over large contact surfaces by numerical simulations. Mar struct 2011;24(4):436–58.

[20] Liu B. Analytical method to assess double-hull ship structures subjected to bulbous bow collision. Ocean Eng 2017;142:27–38.

[21] Ehlers S, Broekhuijsen J, Alsos HS, Biehl F, Tabri K. Simulating the collision response of ship structures: a failure criteria benchmark study. Int Shipbuild Prog 2008;55:127–44.

[22] Marinatos JN, Samuelides MS. Towards a unified methodology for the simulation of rupture in collision and grounding of ships. Mar struct 2015;42:1–32.

[23] Calle MAG, Verleysen P, Alves M. Benchmark study of failure criteria for ship collision modeling using purpose-designed tensile specimen geometries. Mar struct 2017;53:68–85.

[24] Alsos HS, Amdahl J, Hopperstad OS. On the resistance to penetration of stiffened plates, Part II: Numerical analysis. Int J Impact Eng 2009;36(7):875–87.

[25] Villavicencio R, Guedes Soares C. Numerical plastic response and failure of a pre-notched transversely impacted beam. Ships Offshore Struct 2012;7(4):417–29.

[26] Ling Y. Uniaxial true stress-strain after necking. AMP J Technol 1996;5:37–48.

[27] Voce E. A practical strain-hardening function. Acta Metall 1948;51:219–26.

[28] Villavicencio R, Liu B, Guedes Soares C. Experimental and numerical analysis of a tanker side panel laterally punched by a knife edge indenter. Mar struct 2014;37:173–202.

[29] Liu B, Guedes Soares C. Experimental and numerical analysis of the crushing behaviour of stiffened web girders. Int J Impact Eng 2016;88:22–38.

[30] Villavicencio R, Guedes Soares C. Impact response of rectangular and square stiffened plates supported on two opposite edges. Thin-walled Struct 2013;68:164–82.

[31] Cerik BC, Shin HK, Cho SR. On the resistance of steel ring-stiffened cylinders subjected to low-velocity mass impact. Int J Impact Eng 2015;84:108–23.

[32] Liu B, Guedes Soares C. Plastic response and failure of rectangular cross-section tubes subjected to transverse quasi-static and low-velocity impact loads. Int J Mech Sci 2015;90:213–27.

[33] Dieter GE. The tension test. In: Bever MB, Copley SM, Shank ME, Wert CA, Wilkes GL, editors. Mechanical Metallurgy, 3rd ed. New York: McGraw-Hill, 1986. p. 275–295

[34] GB/T 706-2008. Hot rolled section steel.

[35] GB/T 5117-1995. Carbon steel covered electrodes.

[36] Zhang M, Liu J, Hu Z. Experimental and numerical analysis of tanker double-hull structures punched by a wedge indenter. In: Guedes Soares C, Garbatov Y, editors. Proceedings of the 6th International conference on marine structures: Lisbon, Portugal; 2017. p. 549–56.

[37] Alsos HS, Amdahl J. On the resistance to penetration of stiffened plates, Part I: Experiments. Int J Impact Eng 2009;36(6):799–807.

[38] Kõrgesaar M, Romanoff J, Remes H, Palokangas P. Experimental and numerical penetration response of laser-welded stiffened panels. Int J Impact Eng 2018;114:78-92.

[39] Liu B, Villavicencio R, Guedes Soares C. Simplified analytical method to evaluate tanker side panels during minor collision incidents. Int J Impact Eng 2015;78:20–33.

[40] Hallquist JO. LS-DYNA theory manual. California, USA: Livermore Software Technology Corporation; 2006. p. 1–680.

[41] Hallquist JO. LS-DYNA keyword user's manual. California, USA: Livermore

Software Technology Corporation; 2013. p. 1–1121.

[42] Kõrgesaar M, Romanoff J. Influence of mesh size, stress triaxiality and damage induced softening on ductile fracture of large-scale shell structures. Mar struct 2014;38:1–17.

[43] Storheim, M, Amdahl, J, Martens, I. On the accuracy of fracture estimation in collision analysis of ship and offshore structures. Mar struct 2015; 44: 254-287.

[44] Ohtsubo H, Wang G. An upper-bound solution to the problem of plate tearing. J Mar Sci Technol 1995;1:46–51.

[45] Lee YW, Woertz JC, Wierzbicki T. Fracture prediction of thin plates under hemi-spherical punch with calibration and experimental verification. Int J Mech Sci 2004;46(5):751–81.

[46] Gong Y, Gao Y, Xie D, Liu J. Deflection and fracture of a clamped plate under lateral indentation by a sphere. Ocean Eng 2015;103:21–30.

[47] Liu B, Villavicencio R, Zhang S, Guedes Soares C. A simple criterion to evaluate the rupture of materials in ship collision simulations. Mar struct 2017;54:92–111.

[48] Kõrgesaar M., 2015. Assumptions and reality: Stress states in uniaxial tension test. In: Guedes Soares C, Shenoi S, editors. Proceedings of the 5th International conference on marine structures: Southampton, UK; 2015. p. 359–64.

[51] Jones N. The credibility of predictions for structural designs subjected to large dynamic loadings causing inelastic behaviour. Int J Impact Eng 2013;53:106–14.

[52]Jones N. Structural impact. Second edition Cambridge University Press; 2012.

[53] Jones N. Structural aspects of ship collisions. In: Jones N, Wierzbicki T, editors. Structural crashworthiness. London, UK: Butterworth & Co (Publishers) Ltd; 1983. p. 308–37 [chapter 11].

[54] Wen HM, Jones N. Experimental investigation of the scaling laws for metal plates struck by large masses. Int J Impact Eng 1993;13(3):485–505.

LIST OF TABLES

Table 1 Principle particulars of the oil tanker.

Table 2 Scantlings of the double hull prototype.

Table 3 Mechanical properties of material.

Table 4 Mechanical properties of the channel steel.

Table 5 Summary of experimental results.

Table 6 Summary of experimental observations.

Table 7 Summary of the numerical results for specimen S-C.

Table 8 Summary of the numerical results for specimen S-W.

TABLES

Table 1

Principle particulars of the oil tanker.

Overall length	Length between perpendiculars	Molded breadth	Depth	Design draught
145.5 m	136.2 m	23 m	12.5 m	8.8 m

Table 2

Scantlings of the double hull prototype.

Structural component	Plate	Stiffeners
Outer plate	12.0 mm	HP.220×11
Inner plate	12.0 mm	HP.220×11
Stringers	10.0 mm	FB.160×10
Web frames	10.0 mm	FB.150×12

Table 3

Mechanical properties of material.

Property	Units	Specimens
Young's modulus	GPa	207
Poisson's ration	-	0.3
Mass Density	kg/m^3	7850
Yield stress	MPa	239
Ultimate tensile strength	MPa	340
Fractures strain	-	0.29
Strength coefficient	MPa	574.6
Strain-hardening index	-	0.196
ε_{plat}	-	0.0189

Table 4

Mechanical properties of the channel steel.

Property	Units	Channel steel GB:18b[41]
Yield strength	MPa	345
Tensile strength	MPa	510-600
Elongation	-	0.22

Table 5

Summary of experimental results.

Specimen		S-C	S-W
Values at first peak	Force [kN]	177.98	123.5
	Penetration [mm]	89.09	36.31
	Energy [kJ]	8.28	2.58
Average values at first tearing process	Force [kN]	20.39	19.37
Values at second peak	Force [kN]	192.02	100.53
	Penetration [mm]	247.25	203.67
	Energy [kJ]	21.33	9.79
Average values at second tearing process	Force [kN]	-	49.15

Table 6

Summary of experimental observations.

Process	Response	Component	Observations
stage 1	deformation	outer stiffened plate	specimen S-W exhibits a higher elastic limit
		outer plate	specimen S-W exhibits greater stretching resistance
		the central stiffener	bending and tension, no tripping is found
		web frame	buckling is found in specimen S-C
	fracture	outer plate	S-C: triggered by tension S-W: initiates from the wedge corners
		stiffeners	S-C: triggered by global bending and tension S-W: triggered by local bending and tension
stage 3	deformation	stiffeners	one fold is generated
	fracture	inner plate	S-C: triggered by tension and folded stiffener S-W: initiates from the wedge corners
stage 2 and stage 4	tearing	side plates	according to the shapes of the indenters
	crack propagation	outer plates	S-C: along the stiffeners; some stiffeners are fractured S-W: according to the shape of the indenter

Table 7

Summary of the numerical results for specimen S-C.

Step	Components	Behavior	Comparison to experiments
a	outer stiffened plate	elastic bending	matched
b		plate: membrane stretching stiffener: bending and tension	matched
c	web frames	buckling	difference in in-plane resistance
d	outer plate	failed due to tension	matched
e	outer central stiffener	failed due to tension and bending	matched
f	inner central stiffener	folding	difference in in-plane resistance
g		failed due to excessive folding	no fracture in experiment
h	inner stiffened plate	plate failed due to fractured stiffener	plate: crack along the stiffener is not matched stiffener: tension failure in experiment

Table 8

Summary of the numerical results for specimen S-W.

Step	Components	Behavior	Compared to experiments
a	outer stiffened plate	elastic bending	matched
b	outer plate	initial fracture due to shearing	difference in resistance force
c		torn open	matched
d	outer stiffeners	failed due to tension and local bending	matched
e	outer stiffened plate	tearing	difference in tearing resistance
	inner stiffeners	folding	difference in in-plane resistance
f	inner stiffeners	tearing	difference in tearing resistance
	inner plate	initial fracture	matched
g	inner plate	torn open	matched

LIST OF FIGURES

Fig. 1. Impact scenario and the scaled double hull.

Fig. 2. Dimensions of the indenters: (a) conical indenter, and (b) wedge indenter with sharp tip.

Fig. 3. Standard dimensions of the tested pieces (ASTM, E8).

Fig. 4. Stress-strain curves.

Fig. 5. Section profile of channel steel.

Fig. 6. Dimensions of the specimen. Dimensions in mm.

Fig. 7. Specimen fabrication process: (a) inner components and surrounded frame are welded by electrode arc welding, (b) laser marking and slot cutting on side plates, and (c) panels and inner components together with the frame are welded by laser welding, and specific locations are strengthened by electrode arc welding.

Fig. 8. Experimental setup.

Fig. 9. Experimental shape of the deformation: (a) specimen S-C, and (b) specimen S-W.

Fig. 10. Experimental impact response.

Fig. 11. Deformation details in specimen S-C: (a) buckling of the web frame, and (b) crack of the central stiffener.

Fig. 12. Initial fracture of the mid stiffener attached to the outer plate: (a) specimen S-C, and (b) specimen S-W.

Fig. 13. Details of finite element model: (a) system components, (b) added thickness at weld seams, and (c) boundary constraints.

Fig. 14. Engineering stress-strain curves from tensile test and numerical simulation.

Fig. 15. Numerical resistance-penetration responses: (a) specimen S-C, and (b) specimen S-W.

Fig. 16. Deformation process of specimen S-C (a-e: front view; f-h: top view). (The contour levels represent equivalent plastic strain.)

Fig. 17. Crack of the central stiffener attached to the inner plate.

Fig. 18. Deformation process of specimen S-W (d: front view; others: top view).

Fig. 19. Energy absorbed by individual components: (a) specimen S-C, and (b) specimen S-W.

Fig. 20. Influence of the welded elements: (a) specimen S-C, (b) specimen S-W.

Fig. 21. Simulation results for uniaxial tension at various mesh size: (a) engineering stress-strain curves, and (b) Barba's law of EPS and GL criteria.

Fig. 22. Resistance-penetration curves with different failure criteria for various element size: (a) EPS, (b) GL, and (c) RTCL. Left: specimen S-C, Right: specimen S-W.

Fig. 23. Fracture shape of inner plate simulated with 8 mm element size: (a) GL and RTCL, and (b) EPS.

Fig. 24. Stress strain curves for different material relations.

Fig. 25. Numerical results for different material relations: (a) specimen S-C, (b) specimen S-W, and (c) deformation shape in specimen S-C when w=0 (front view).

Fig. 26. Resistance-penetration responses for the full-scale prototypes, punched by: (a) conical indenter, (b) knife-edge indenter.

FIGURES

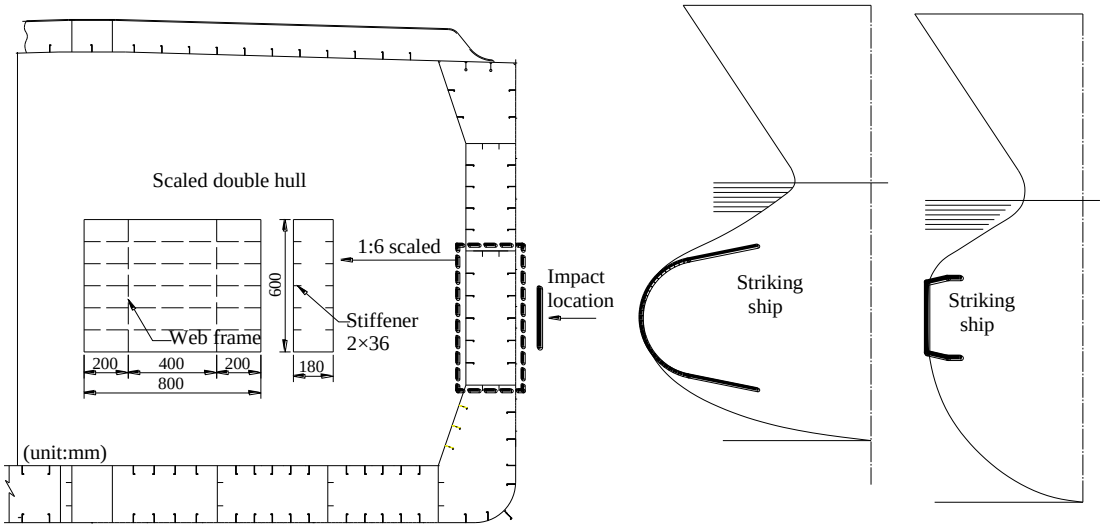

Fig. 1. Impact scenario and the scaled double hull.

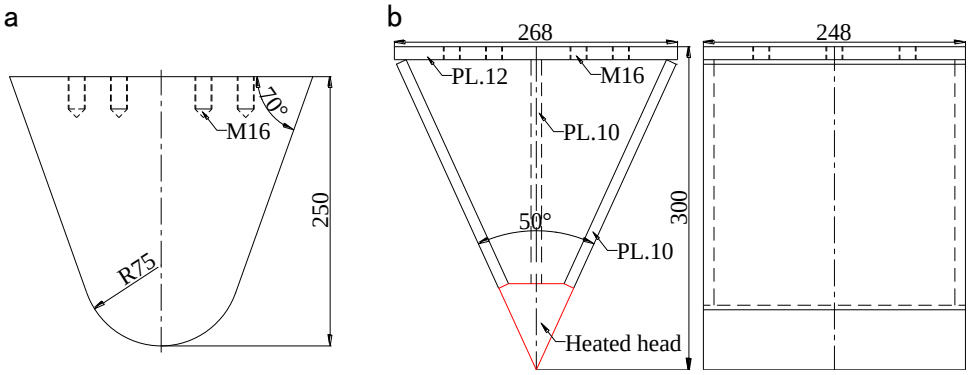

Fig. 2. Dimensions of the indenters: (a) conical indenter, and (b) wedge indenter with sharp tip.

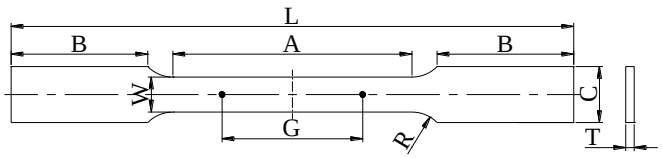

G-Gauge length	50mm
W-Width	12.5mm
T-Thickness	2mm
R-Radius of fillet	12.5mm
L-Overall length	200mm
A-Length of reduced section	85mm
B-Length of grip section	~50mm
C-Width of grip section	20mm

Fig. 3. Standard dimensions of the tested pieces (ASTM, E8).

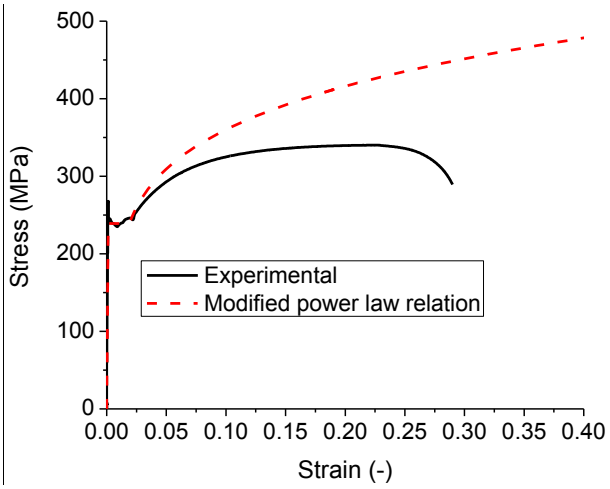

Fig. 4. Stress-strain curves.

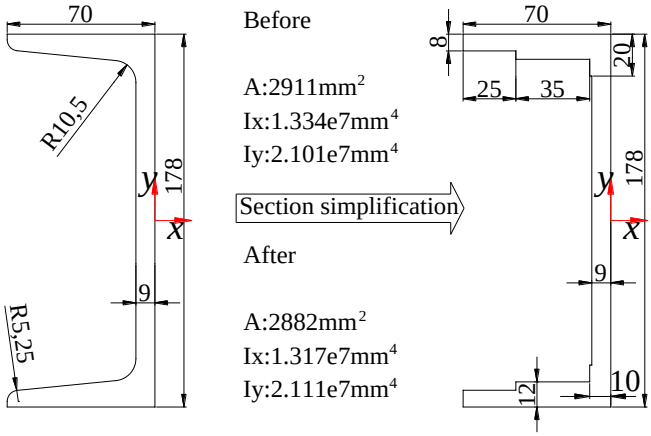

Fig. 5. Section profile of channel steel.

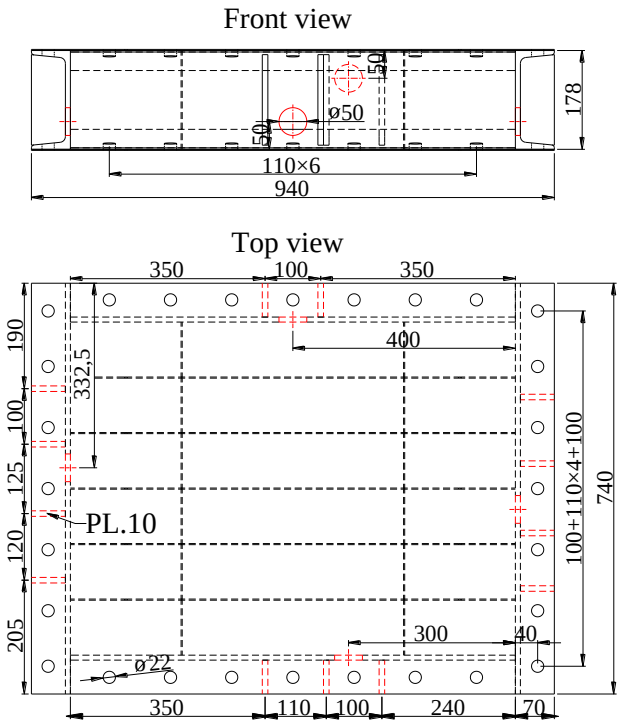

Fig. 6. Dimensions of the specimen. Dimensions in mm.

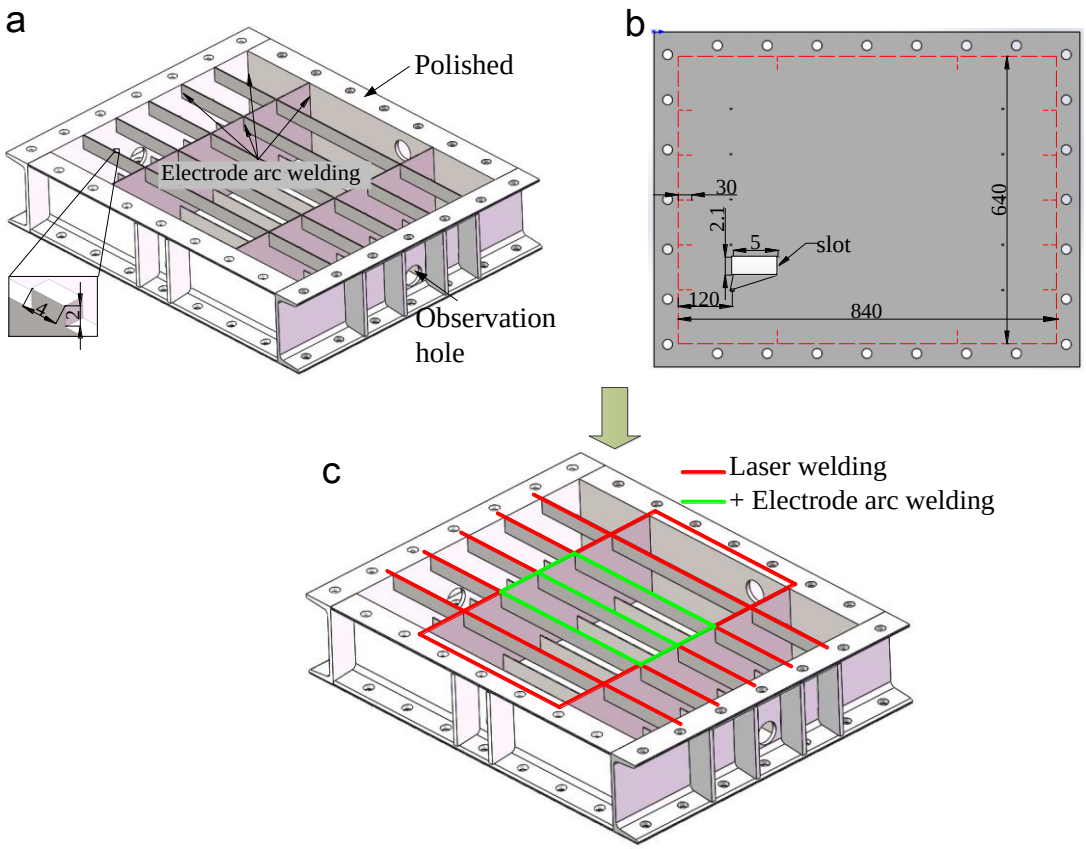

Fig. 7. Specimen fabrication process: (a) inner components and surrounded frame are welded by electrode arc welding, (b) laser marking and slot cutting on side plates, and (c) panels and inner components together with the frame are welded by laser welding, and specific locations are strengthened by electrode arc welding.

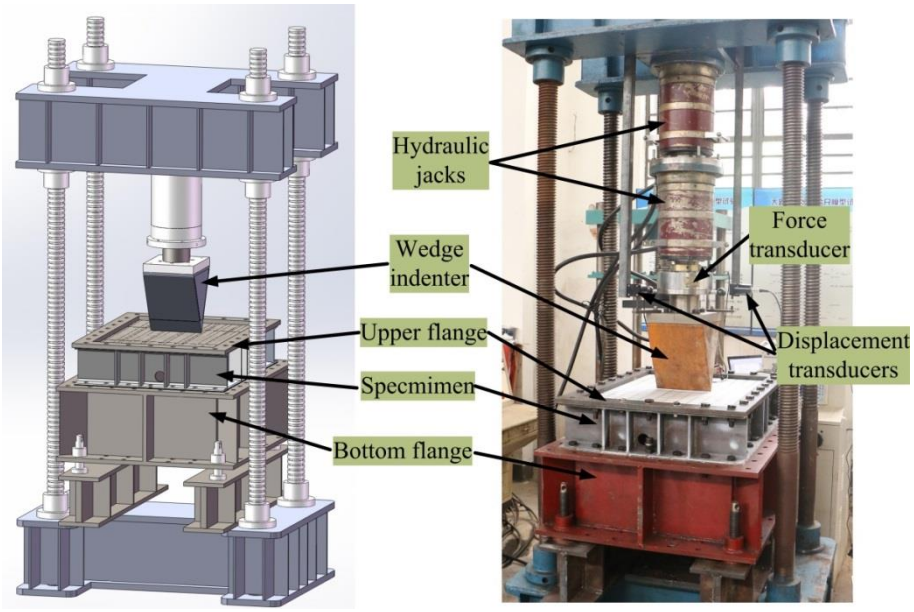

Fig. 8. Experimental setup.

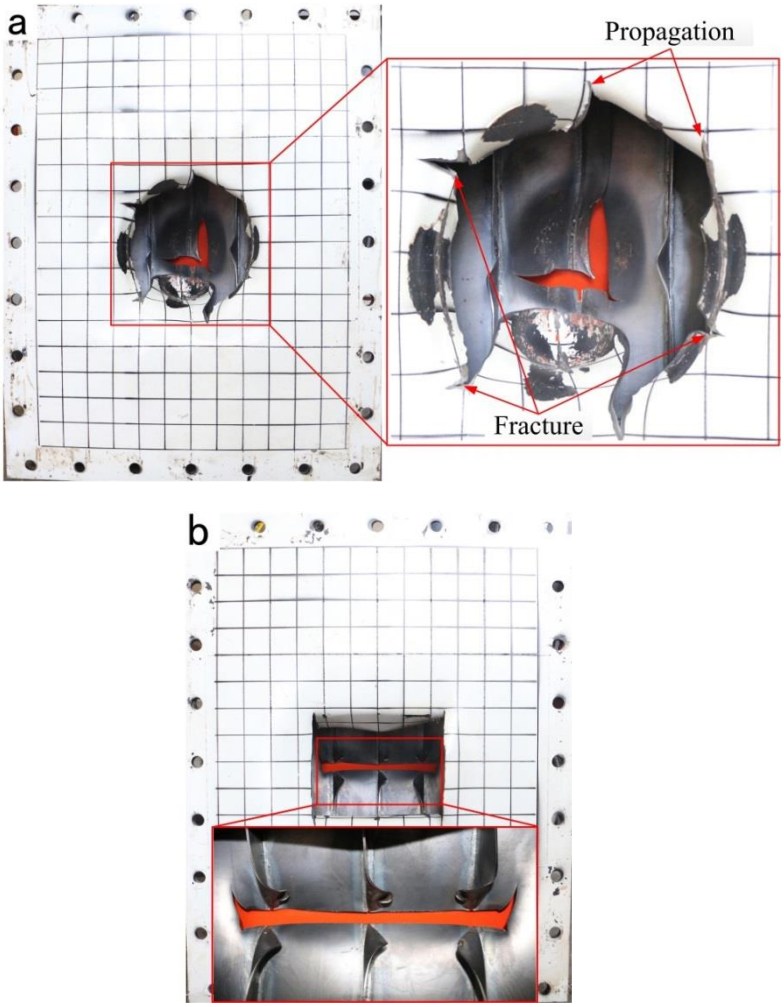

Fig. 9. Experimental shape of the deformation: (a) specimen S-C, and (b) specimen S-W.

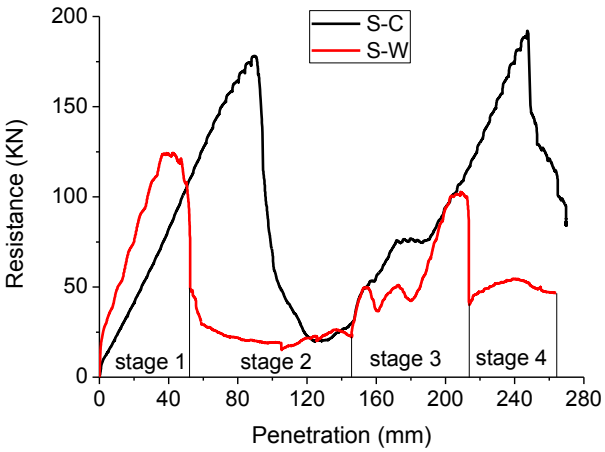

Fig. 10. Experimental impact response.

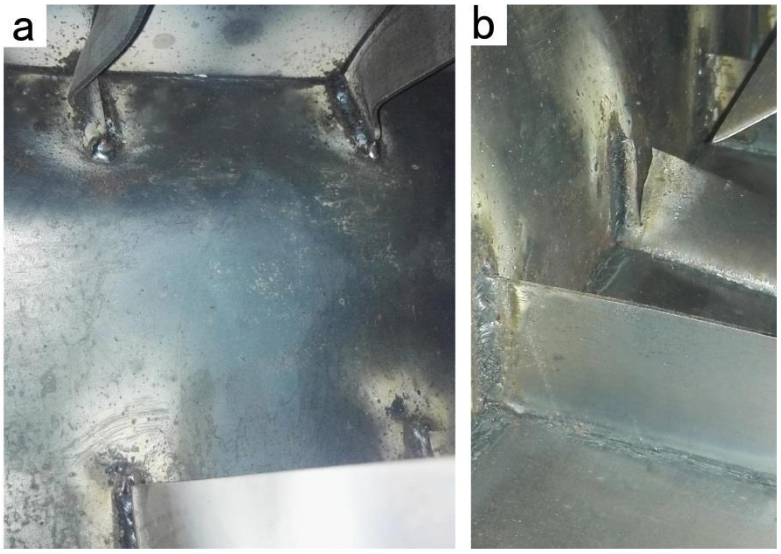

Fig. 11. Deformation details in specimen S-C: (a) buckling of the web frame, and (b) crack of the central stiffener.

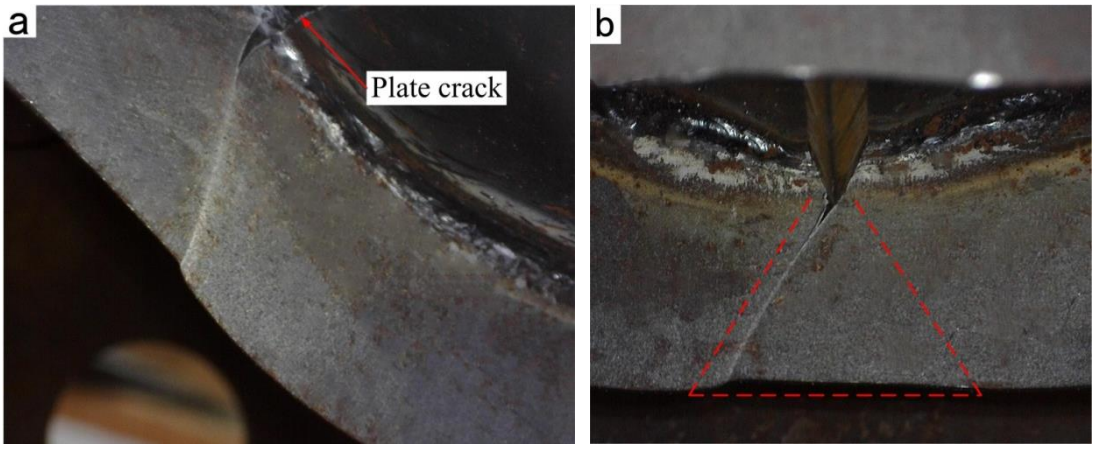

Fig. 12. Initial fracture of the mid stiffener attached to the outer plate: (a) specimen S-C, and (b) specimen S-W.

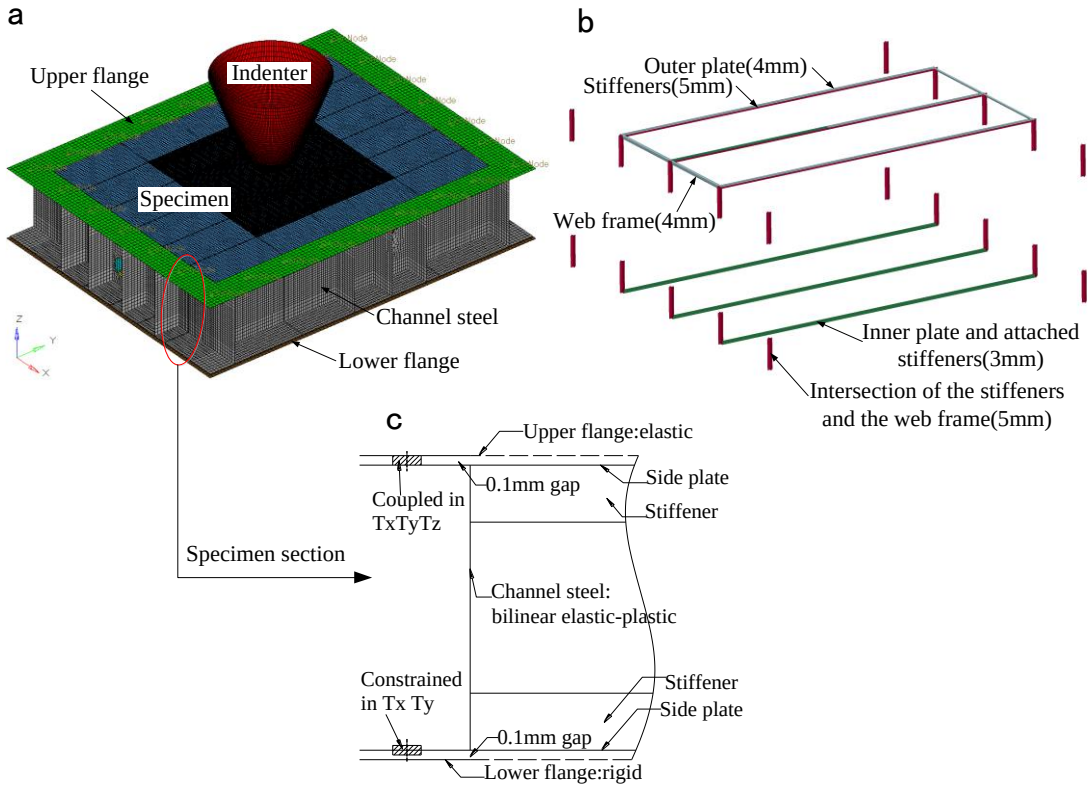

Fig. 13. Details of finite element model: (a) system components, (b) added thickness at weld seams, and (c) boundary constraints.

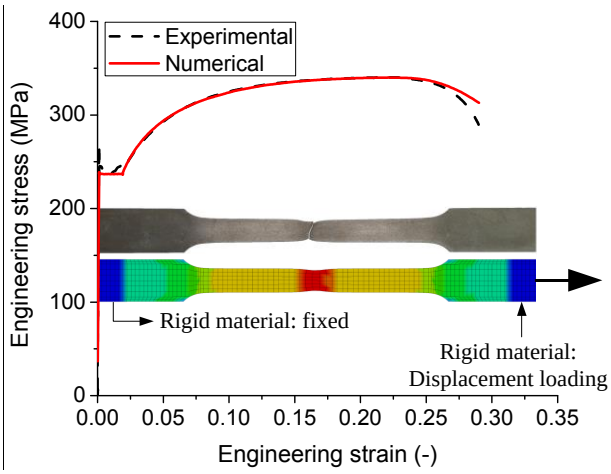

Fig. 14. Engineering stress-strain curves from tensile test and numerical simulation.

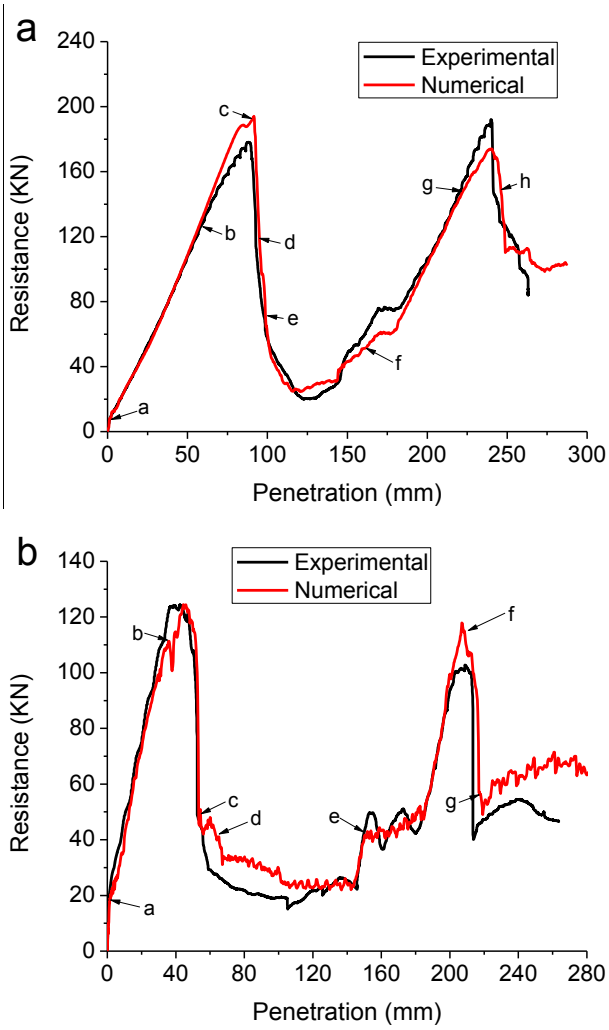

Fig. 15. Numerical resistance-penetration responses: (a) specimen S-C, and (b) specimen S-W.

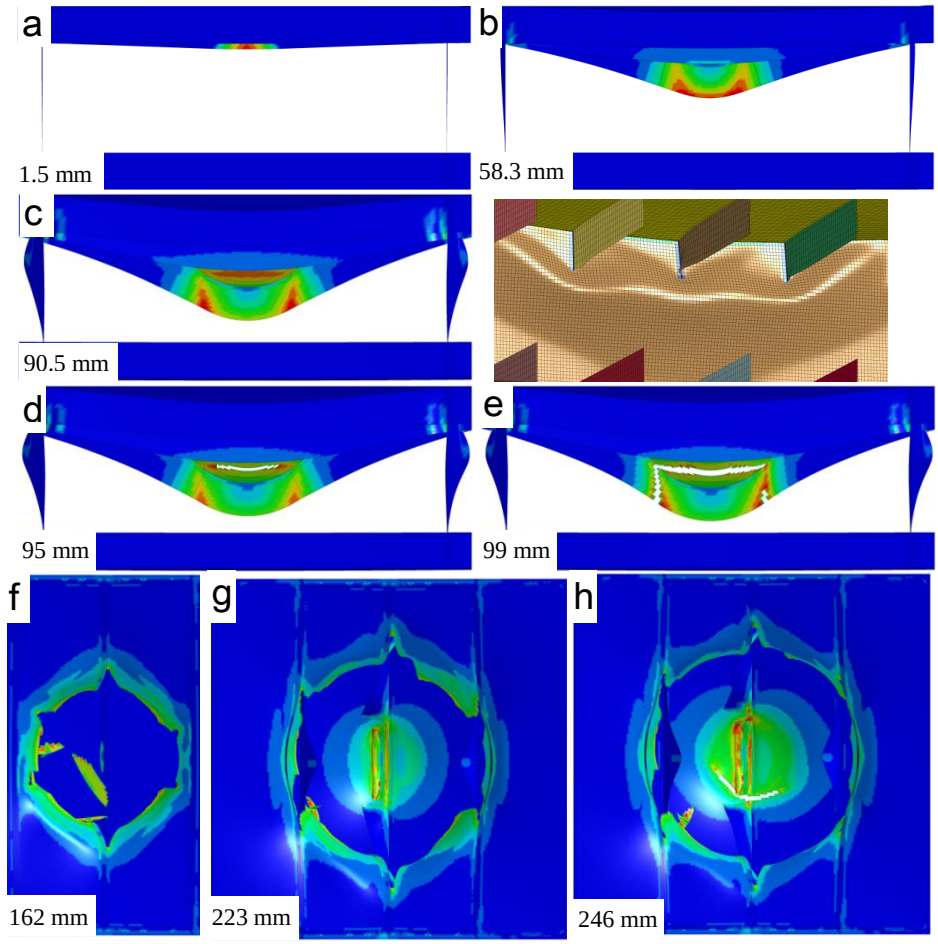

Fig. 16. Deformation process of specimen S-C (a-e: front view; f-h: top view). (The contour levels represent equivalent plastic strain.)

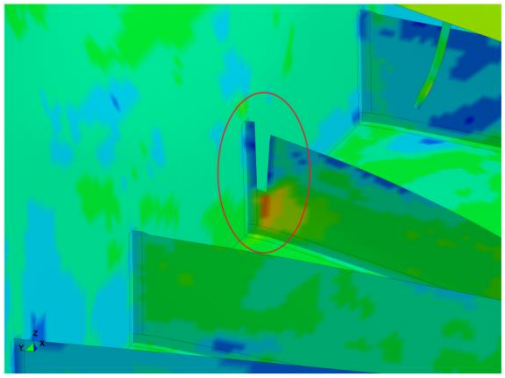

Fig. 17. Crack of the central stiffener attached to the inner plate.

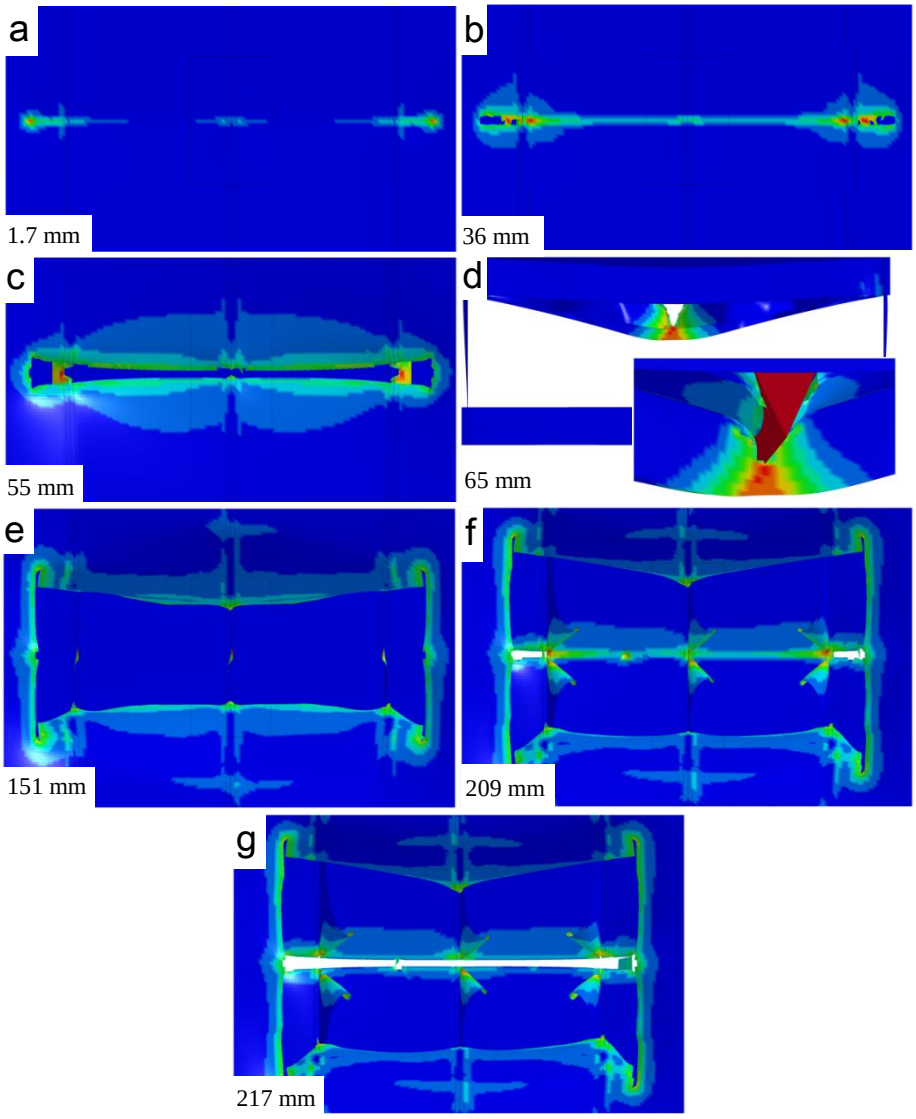

Fig. 18. Deformation process of specimen S-W (d: front view; others: top view).

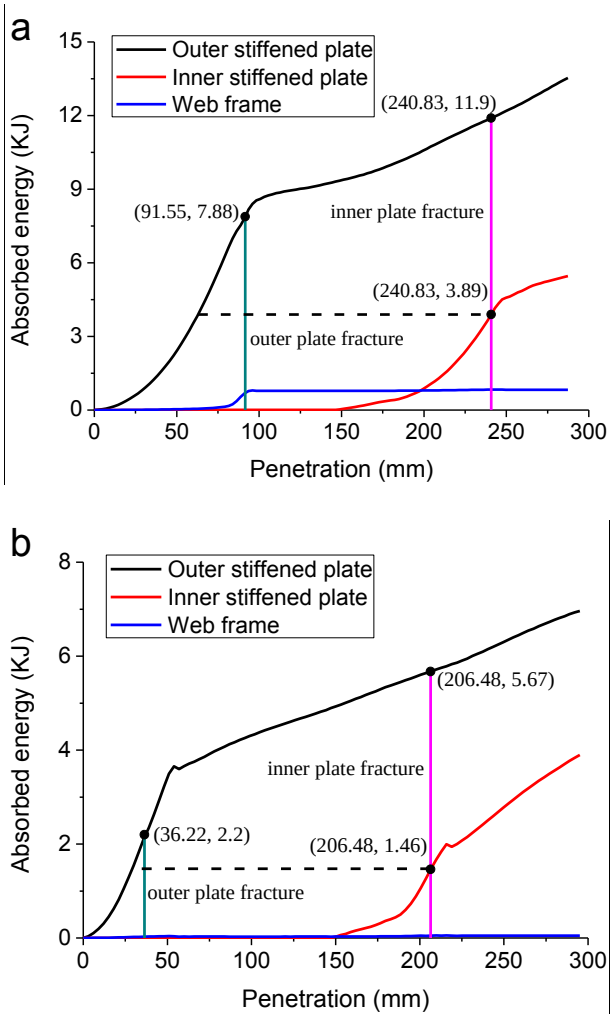

Fig. 19. Energy absorbed by individual components: (a) specimen S-C, and (b) specimen S-W.

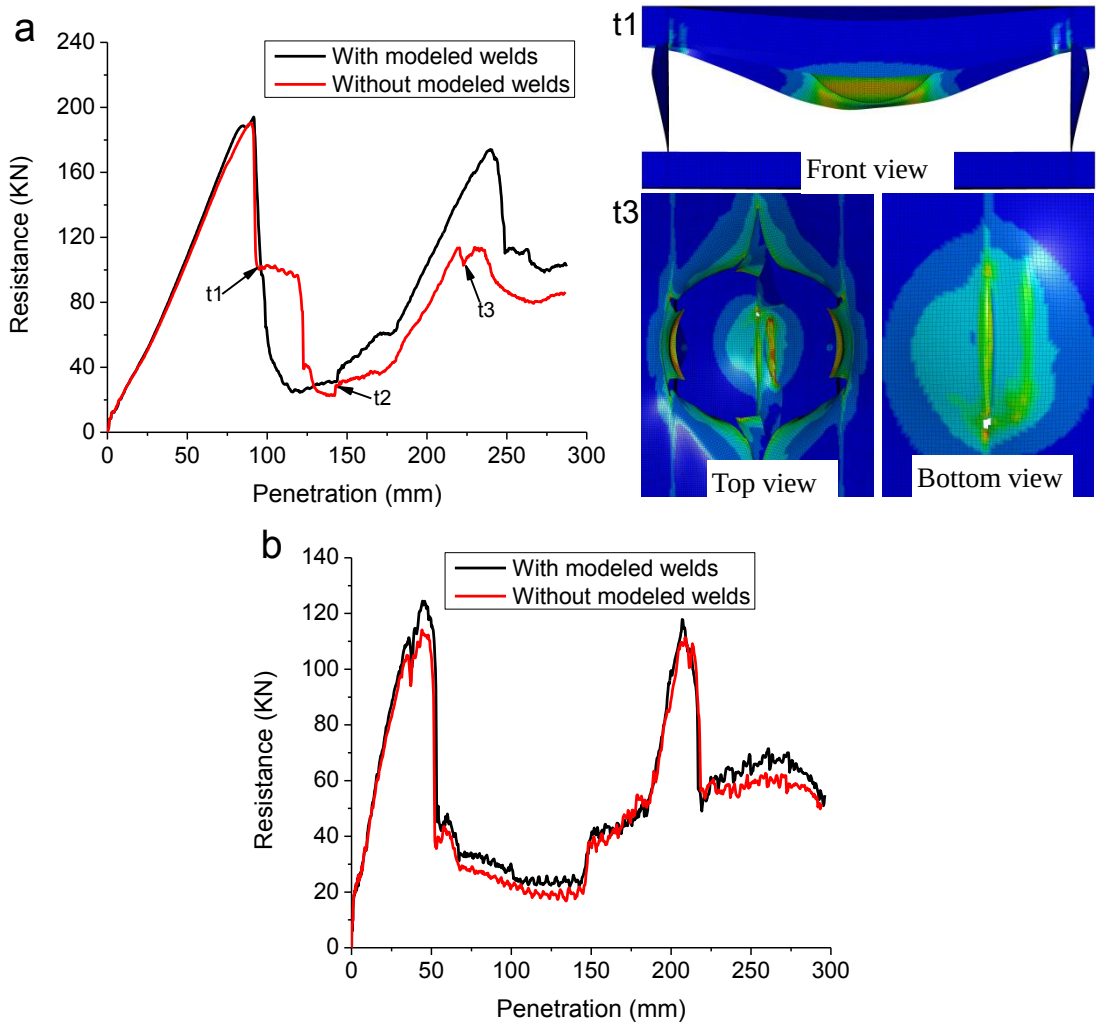

Fig. 20. Influence of the welded elements in scaled model: (a) specimen S-C, (b) specimen S-W.

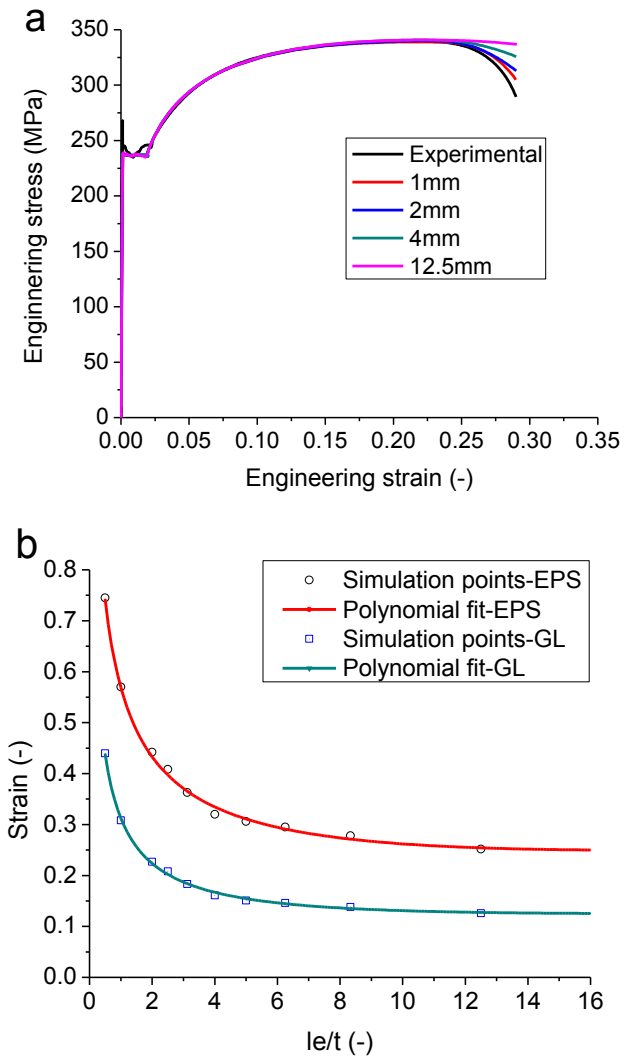

Fig. 21. Simulation results for uniaxial tension at various mesh sizes: (a) engineering stress-strain curves, and (b) Barba's law of EPS and GL criterion.

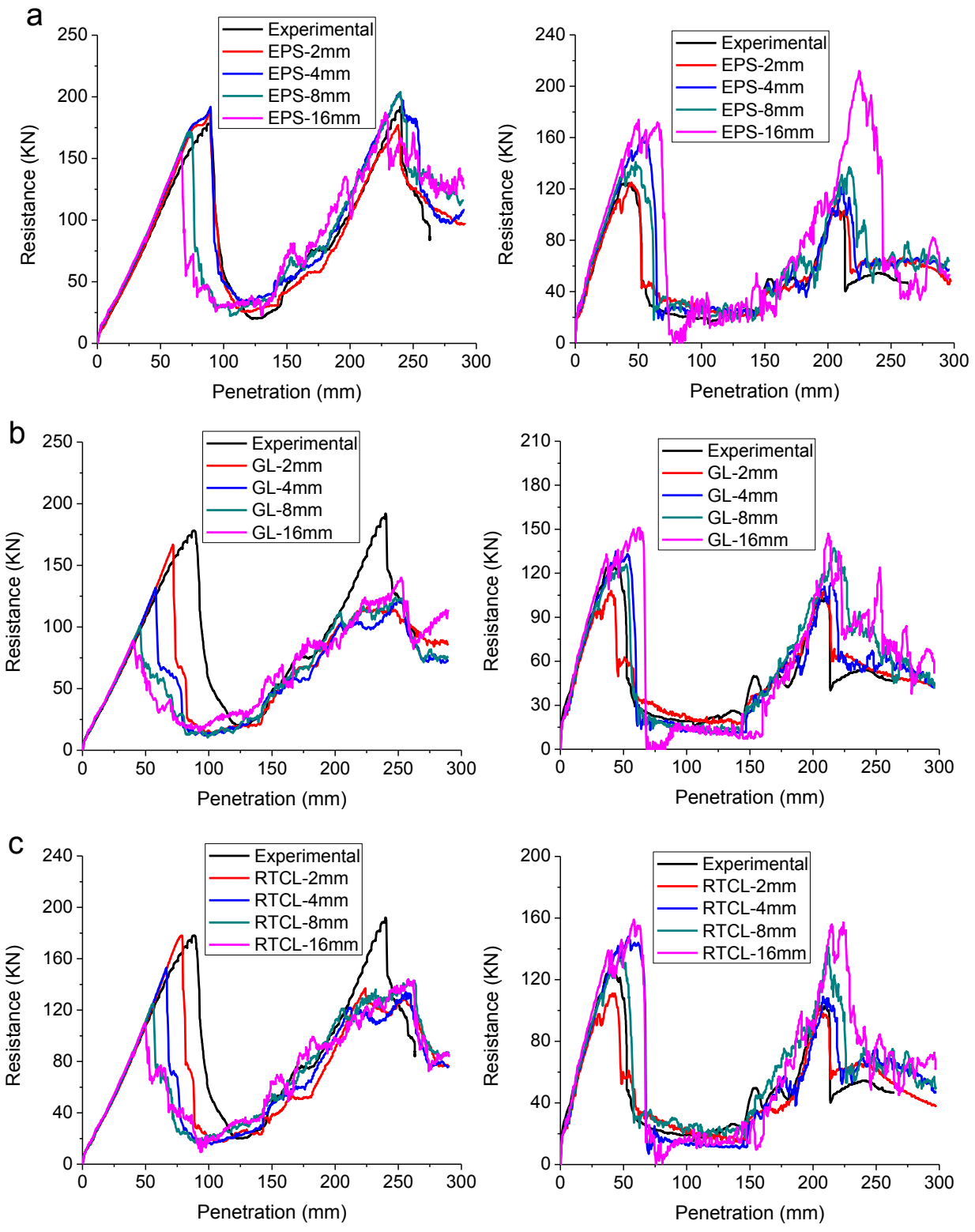

Fig. 22. Resistance-penetration curves with different failure criteria with various element sizes: (a) EPS, (b) GL, and (c) RTCL. Left: specimen S-C, Right: specimen S-W.

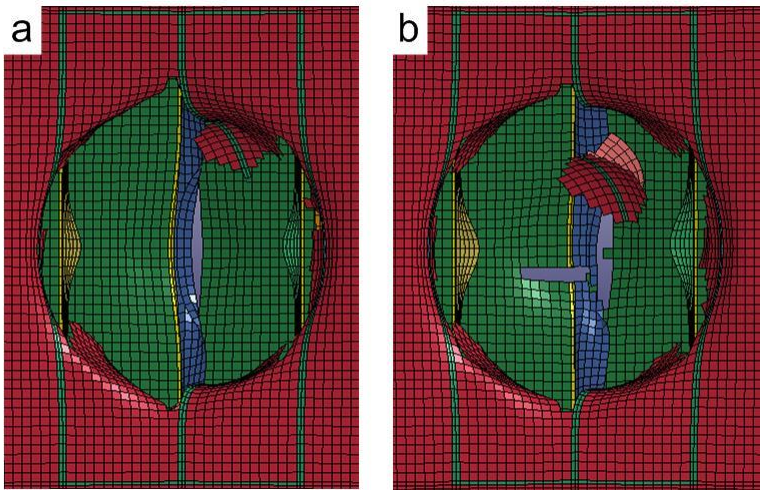

Fig. 23. Fracture shape of inner plate simulated with 8 mm element size: (a) GL and RTCL, and (b) EPS.

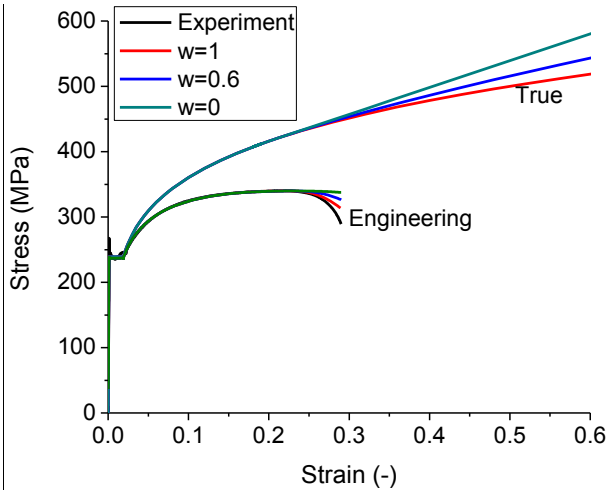

Fig. 24. Stress strain curves for different material relations.

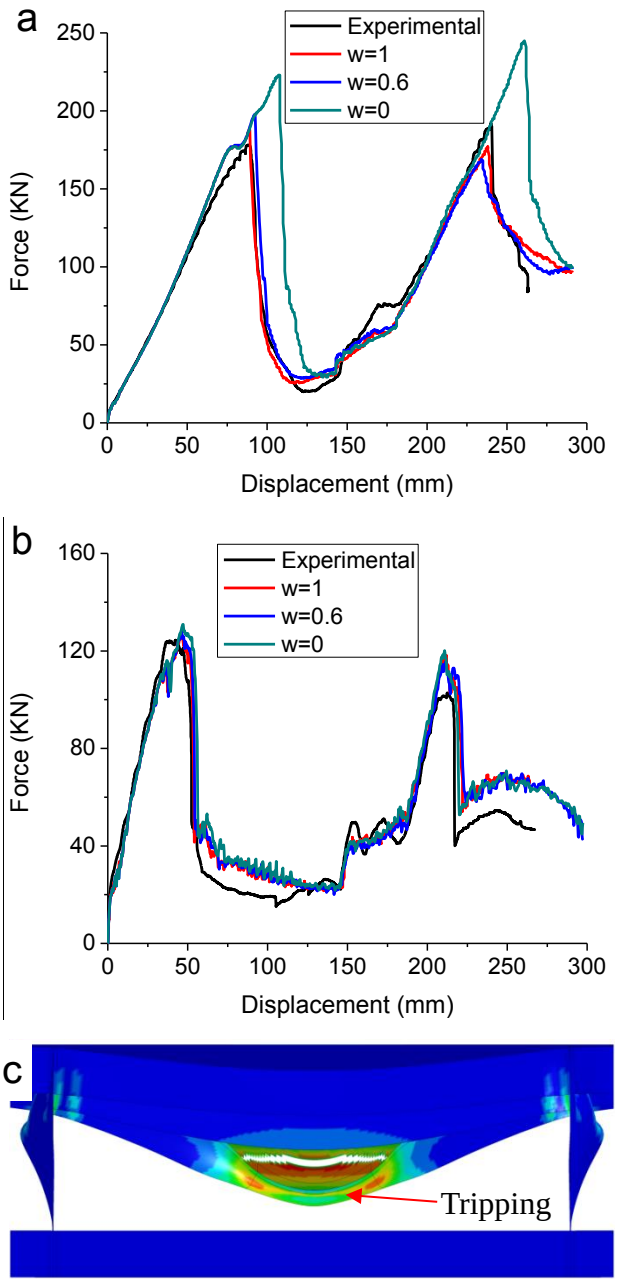

Fig. 25. Numerical results for different material relations: (a) specimen S-C, (b) specimen S-W, and (c) deformation shape in specimen S-C when *w*=0 (front view).

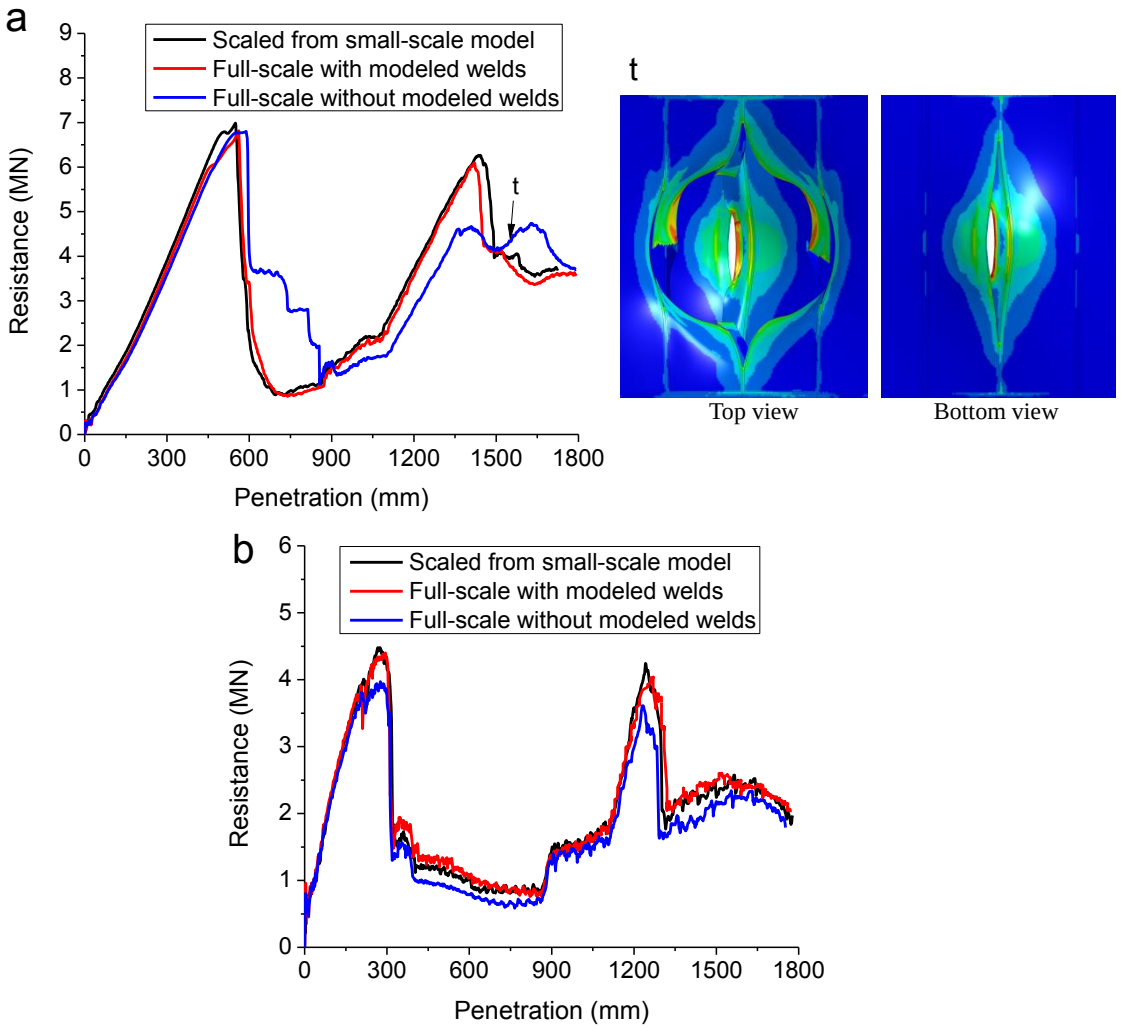

Fig. 26. Resistance-penetration responses for the full-scale prototype, punched by: (a) conical indenter, (b) knife-edge indenter.